# Assessment of a Nonlinear Unsteady Vortex Lattice-Vortex Particle Method for Predicting Helicopter Rotor/Multirotor Aerodynamics

Jinbin Fu \* and Eric Laurendeau<sup>†</sup>
Polytechnique Montréal, Montréal, Quebec, Canada, H3T 1J4

This study presents a nonlinear unsteady vortex lattice-vortex particle method (NL-UVLM-VPM) for the efficient prediction of helicopter rotor aerodynamics. The approach couples a nonlinear unsteady vortex lattice method for aerodynamic modeling with a mesh-free vortex particle method for wake evolution. Nonlinear viscous effects, derived from two-dimensional Reynolds-Averaged Navier-Stokes (RANS) sectional data, are incorporated through a low-cost viscous-inviscid  $\alpha$ -coupling algorithm. To stabilize wake development, the Vreman eddy-viscosity subgrid-scale model is integrated with the particle strength exchange (PSE) method within a large eddy simulation (LES) framework, enabling robust and accurate resolution of the wake coherent, transient, and turbulent breakdown regions. The solver further includes a novel adaptive particle conversion technique, reducing computational wall-clock time by nearly 70%, and a multiple-reference-frame kinematics formulation, allowing simulations of complex flight conditions such as forward flight and multi-rotor interactions. Validation against experimental and unsteady RANS (URANS) data for three representative benchmark cases shows good agreement in aerodynamic loads and wake structures. Moreover, the NL-UVLM-VPM achieves comparable accuracy to URANS, with over two orders of magnitude reduction in computational cost, demonstrating its potential as a reliable and efficient tool for rotorcraft aerodynamic studies.

#### **Nomenclature**

AIC = aerodynamic influence coefficient matrix

A = area of the vortex ring,  $m^3$ 

a = Oseen parameter

 $C_D$  = airfoil drag coefficient,  $D/(1/2)\rho U_{\infty}^2 c$ 

 $C_L$  = airfoil lift coefficient,  $L/(1/2)\rho U_{\infty}^2 c$ 

<sup>\*</sup>Post-doctoral fellow, Department of Mechanical Engineering, Polytechnique Montréal, jinbin.fu@polymtl.ca, jinbin.fu@polimi.it.
†Professor, Department of Mechanical Engineering, Polytechnique Montréal, eric.laurendeau@polymtl.ca, AIAA Senior Member

 $C_P$  = sectional pressure coefficient,  $P/(1/2)\rho U_{\infty}^2$ 

 $C_Q$  = torque coefficient,  $T/\rho U_{\infty}^2 \pi R^3$ 

 $C_T$  = thrust coefficient,  $T/\rho U_{\infty}^2 \pi R^2$ 

c = chord length, m

 $c_S$  = the standard Smagorinsky subgrid-scale model coefficient

 $c_V$  = the standard Vreman subgrid-scale model coefficient

dl = vector length of the straight-line vortex segment, m

 $\mathbf{F}_{i}$  = force on the vortex ring element, N

K = Biot-Savart kernel,  $K(\rho)$ 

M = Mach number

 $N_{rev}$  = number of rotor revolutions

 $N_b$  = number of blades per rotor

 $N_p$  = number of vortex particles

 $\mathbf{n}_{i}$  = the normal vector of the *i*-th vortex ring

 $n_i$  = number of particles assigned at the *i*-th straight-line element

 $n_t$  = number of particles assigned at the tip vortex segment

R = rotor radius, m

 $R_c$  = cut-out rotor radius, m

Re = Reynolds number

 $Re_v$  = vortex Reynolds number

r = radius position, m

**r** = vector from the collocation point to the ends of the vortex segment, m

 $r_c$  = vortex core radius, m

 $r_{c_0}$  = initial vortex core radius, m

T = rotor thrust, N

t = time, s

u = velocity, m/s

V = volume of vortex particle,  $m^3$ 

 $\mathbf{x}_{i}$  = the position of the *i*-th particle,  $\mathbf{x}_{i}(t)$ , m

 $\phi$  = velocity potential, m<sup>2</sup>/s

 $\mu_{\rm L}$  = doublet strength

 $\sigma_{\rm L}$  = source strength

```
\alpha = angle of attack, deg
```

 $\alpha_{ij}$  = Vreman SGS model parameter

 $\psi$  = azimuthal angle, deg

 $\theta$  = blade pitch angle, deg

 $\beta$  = blade flap angle, deg

 $\beta_{ij}$  = Vreman SGS model parameter

 $\delta$  = blade lead-lag angle, deg

 $\Delta_m$  = filter width at the particle level, m

 $\Gamma$  = circulation,  $m^2/s$ 

 $\Gamma_{\rm p}$  = vortex strength of p th particle,  $\Gamma_{\rm p}(t)$ , m<sup>3</sup>/s

 $\rho$  = 3D Gaussian smoothing function parameter

 $\rho_{\infty}$  = air density, kg/m<sup>3</sup>

 $\sigma$  = filter width (smoothing radius or core size), m

 $\zeta_{\sigma}$  = 3D Gaussian distribution,  $1/m^2$ 

 $\nu$  = kinematic viscosity, m<sup>2</sup>/s

 $\omega$  = vorticity field,  $\omega(\mathbf{x}, t)$ , 1/s

# Subscripts

LES = large-eddy simulation

PSE = particle strength exchange

ind = induced

inv = inviscid

tur = turbulent

vis = viscous

 $\infty$  = freestream

# I. Introduction

Modeling helicopter rotor and multirotor aerodynamics accurately and efficiently remain a significant challenge due to the highly complex aerodynamic environment of rotor systems. With increasing interest in urban air mobility (UAM), there is a growing demand for aerodynamic tools that can offer a balance between fidelity and computational cost. High-fidelity tools, such as 3D Unsteady Reynolds-Averaged Navier-Stokes (URANS) and Scale-Resolving Simulation (SRS) methods, rely on high-density grids to overcome numerical dissipation. However, these methods are computationally intensive and often have limited effectiveness in preserving the vortex structure. For

example, in [1], the ROSITA 3D URANS solver was used to simulate the forward flight of the HART-II main rotor. The simulation used 12.6 million cells and ran on 80 cores, requiring 2978 CPU hours per revolution. However, the captured vortex wakes were less than satisfactory. Similarly, Chaderjian and Ahmad [2] simulated the hovering UH-60 main rotor using the Detached Eddy Simulation (DES) technique in the OVERFLOW CFD code. The simulation involved 78 million grid points and 1536 cores, taking 8909 CPU hours per revolution. From an engineering accuracy perspective, satisfactorily resolving rotor wakes typically requires 40 to 90 million cells, with simulations that consume 4 to 5 days on 240-512 cores for fewer than 15 rotor revolutions [3, 4].

In recent years, increasing research efforts have been directed towards developing mid-fidelity aerodynamic tools that achieve a better balance between accuracy and computational efficiency [5–9], particularly for the conceptual design stage. These tools are capable of simulating tens of rotor revolutions in affordable CPU hours and providing reliable solutions on a personal computer. They typically combine potential flow methods for rotor blade analysis with vortex methods for rotor wake modeling, providing a practical solution for engineering applications.

The lifting-line, unsteady vortex-lattice, and unsteady panel methods are the three most representative potential flow approaches for predicting rotor aerodynamic loads in medium-fidelity aerodynamic tools. The lifting-line method is a one-dimensional (1D) model of thin, slender lifting surfaces with straight-line vortex elements distributed along the blade span to enable circulation to vary across them. The unsteady vortex-lattice method extends this approach to a two-dimensional (2D) surface model, representing the blade as zero-thickness vortex rings with circulation varying in both the spanwise and chordwise directions. In contrast, the unsteady panel method employs source and doublet panels to account for blade thickness, placing panels on both the upper and lower sides of the blade instead of the thin camber surface assumed in the vortex-lattice method. However, these methods are limited to incompressible, inviscid, and irrotational flows. Consequently, nonlinear effects on the blade, such as viscous effects, compressibility, sweep cross-flow (2.5D), transonic flow, and ice accretion, fail to be predicted due to underlying assumptions. To address these limitations, such complex nonlinear aerodynamic behaviors have traditionally been incorporated into calculations using a simple table-based look-up method [10] or nonlinear (NL) coupling algorithms [7, 11–13].

The simple look-up method, which retrieves aerodynamic coefficients from a 2D aerodynamic database, is well-suited for simulating rotors in hover, as time iterations effectively mimic nonlinear sub-iterations. However, this approach cannot accurately capture variations in downwash induced by changes in lift within a time step for each blade section, making it less appropriate for rotors in forward and maneuvering flight simulations. This issue may be bypassed through the adoption of nonlinear coupling algorithms. In these approaches, nonlinear correction was applied by changing either the local circulation  $\Gamma$  or the local angle of attack  $\alpha$ , referred to as the  $\Gamma$ -based method and the  $\alpha$ -based method, respectively. However, the  $\Gamma$ -based method is less robust, as it relies on under-relaxation to achieve convergence and fails in the post-stall region. In contrast, the  $\alpha$ -based coupling method is generally preferred, as it remains effective in the post-stall region and requires significantly less relaxation [14]. In recent years, several researchers have employed

nonlinear coupling algorithms to improve the accuracy of aerodynamic predictions for rotors. For instance, Lee *et al.* [7] implemented a  $\Gamma$ -based coupling method, using an arbitrary control point along the blade chordwise direction to compute the induced velocities and determine the effective angle of attack. Proulx-Cabana [11] *et al.* and Samad [13] *et al.* applied a modified  $\alpha$ -method that eliminates the dependency on the viscous slope, effectively integrating the unsteady vortex-lattice method with a 2D RANS database.

For rotor wake modeling in medium-fidelity tools, both the free-wake method and the vortex particle method (VPM) have been employed to capture complex rotor wake structures. However, the potential flow assumption prevents the free-wake models from obtaining reliable aerodynamic predictions, as they rely heavily on empirical parameters such as vortex decay factor, vortex core size, and wake roll-up [15]. Furthermore, numerical convergence issues may arise for interacting wake panels or those approaching the ground due to challenges with panel stretching and deformation [16]. As an alternative, VPM can effectively address these problems by representing wake panels as vortex particles convected in a Lagrangian framework, thus eliminating the numerical dissipation inherent in Eulerian CFD methods and improving predictive accuracy and computational efficiency. Consequently, in recent years, the development of mid-fidelity tools using VPM has become popular in conceptual design due to the growing need to predict complex aerodynamic interactions in UAM at an affordable computational cost. For example, Politecnico di Milano developed DUST [8], an open-source tool with multiple potential flow methods and VPM to analyze complex electric vertical take-off and landing (eVTOL) configurations. Similarly, Brigham Young University created FlowUnsteady [9], an open-source variable-fidelity framework based on the reformulated VPM to study rotor-rotor interactions and analyze the aerodynamics of complete eVTOL configurations.

Despite its increasing popularity, the VPM is numerically unstable due to the vortex stretching instability caused by inadequate compensation for viscous diffusion at sub-grid scales, which leads to the core-overgrowth problem. Various approaches have been adopted to mitigate this numerical challenge in turbulent modeling, especially in rotor wake simulations. For instance, Zhao and He [5] employed the particle strength exchange (PSE) method to solve the viscous diffusion term and used an adaptive particle splitting/merging/deleting algorithm to alleviate excessive particle growth. Alvarez and Ning [9, 10] reformulated the VPM to improve numerical stability. They developed a dynamic subfilter-scale (SFS) vortex stretching model applied directly to the vortex stretching term and coupled the core spreading method (CSM) with radial basis function (RBF) interpolation for viscous diffusion, achieving numerical stability. Valentin and Bernardos [17] compared the PSE, CSM, and diffusion velocity method (DVM) to analytical solutions in 2D Lamb-Oseen vortex and 3D vortex ring cases, finding that the DVM performed better than the other two schemes in long-term simulations and wake decay analysis.

This work presents a mid-fidelity rotor aerodynamics prediction solver that differs from other mid-fidelity tools, such as DUST and FlowUnsteady. It combines a nonlinear unsteady vortex-lattice method (NL-UVLM) with a VPM solver for fast and effective aerodynamic simulations of helicopter rotors. In particular, this tool employs a computationally

efficient viscous-inviscid  $\alpha$ -coupling algorithm, supported by a 2D RANS database from the in-house flow solver CHAMPS (CHapel Multi-Physics Simulation) [18], to facilitate nonlinear correction. Additionally, it integrates the Vreman eddy viscosity subgrid-scale (SGS) model with the PSE method within a LES framework to solve viscous diffusion and improve the stability of wake development.

A previous study [19] evaluated the method's capability to predict the hover performance of a scaled S-76 rotor model from the 2nd AIAA Rotorcraft Hover Prediction Workshop through comparison with literature data. However, that study focused solely on the hovering S-76 rotor without quantifying the computational efficiency or assessing the general applicability of the method to more complex flight regimes or multi-rotor interaction scenarios. In the present work, the tool is further developed and generalized to simulate forward flight, including blade-vortex interaction (BVI), as well as aerodynamic interference effects between rotors. Several algorithmic enhancements have been incorporated, such as an adaptive wake-particle conversion method and a multiple-reference-frame kinematic formulation, which improve computational performance and facilitate the treatment of complex rotor-blade motions. The developed solver is systematically assessed against experimental and high-fidelity URANS data through three representative benchmark cases.

This paper is organized as follows. Section II describes the numerical implementations of the NL-UVLM and VPM solvers, the coupling strategy to connect the NL-UVLM and VPM methods, the multiple-reference-frame formulation for rotor-blade kinematics, the in-house CFD solver – CHAMPS for generating the 2D airfoil aerodynamic database, and ROSITA for high-fidelity URANS rotor flow validation. In Section III, the results obtained with our developed mid-fidelity solver for the selected benchmark test cases, along with comparisons against URANS simulations and experimental measurements, are presented. Furthermore, the computational efficiency of the tool is also outlined in Section III. Finally, the main conclusions of this study are summarized in Section IV.

#### **II. Numerical Methods**

#### A. Nonlinear unsteady vortex-lattice method (NL-UVLM)

The flow surrounding rotorcraft is assumed to be inviscid, incompressible, and irrotational. Thus, a velocity potential  $\phi$  can be defined, and the continuity equation for  $\phi$  in the inertial reference frame becomes the Laplace equation:

$$\nabla^2 \phi = 0 \tag{1}$$

using Green's identity, the integral solution to the Laplace equation is expressed by summing up the source  $\sigma_L$  and doublet  $\mu_L$  distributions over the body surface  $S_B$ :

$$\phi(\mathbf{x}) = \frac{-1}{4\pi} \int_{S_R} \left[ \sigma_L \left( \frac{1}{r} \right) - \mu_L \mathbf{n} \cdot \nabla \left( \frac{1}{r} \right) \right] dS(\mathbf{y})$$
 (2)

where r is the distance between  $\mathbf{x}$  and  $\mathbf{y}$ , and  $\mathbf{n}$  is the outward unit normal vector of the body surface  $S_B$ . When the body surface  $S_B$  is discretized into zero-thickness vortex sheets with negligible source strength  $\sigma$ , and the impermeable Neumann boundary condition is applied to Eq. (2), the vortex lattice method (VLM) is obtained. The resulting integral equation can be derived as

$$\left\{ \int_{S_B} \mu_L \mathbf{n} \cdot \nabla \left( \frac{1}{r} \right) dS - \mathbf{V}_{S_B} + \mathbf{V}_{\infty} + \mathbf{V}_{\text{wake}} \right\} \cdot \mathbf{n} = 0$$
 (3)

where  $V_{S_B}$  is the body surface velocity, and  $V_{wake}$  is the velocity induced by the wake.

As shown in Fig. 1, in rotor simulations, the blade geometry is treated as a thin body composed of lifting surfaces, and the wake is represented as a set of vortex panels. The blade and wake are simulated using the classical vortex-lattice method [20] with time-stepping, referred to as the unsteady vortex-lattice method (UVLM). Specifically, the blade planform is simplified to a flat surface between the leading and trailing edges, discretized using a structured grid. Vortex ring elements are placed at the quarter-chord location of each grid element. For the wake, vortex panels extend from the trailing edge to infinity, with the Kutta condition applied to ensure that the circulation equals zero.

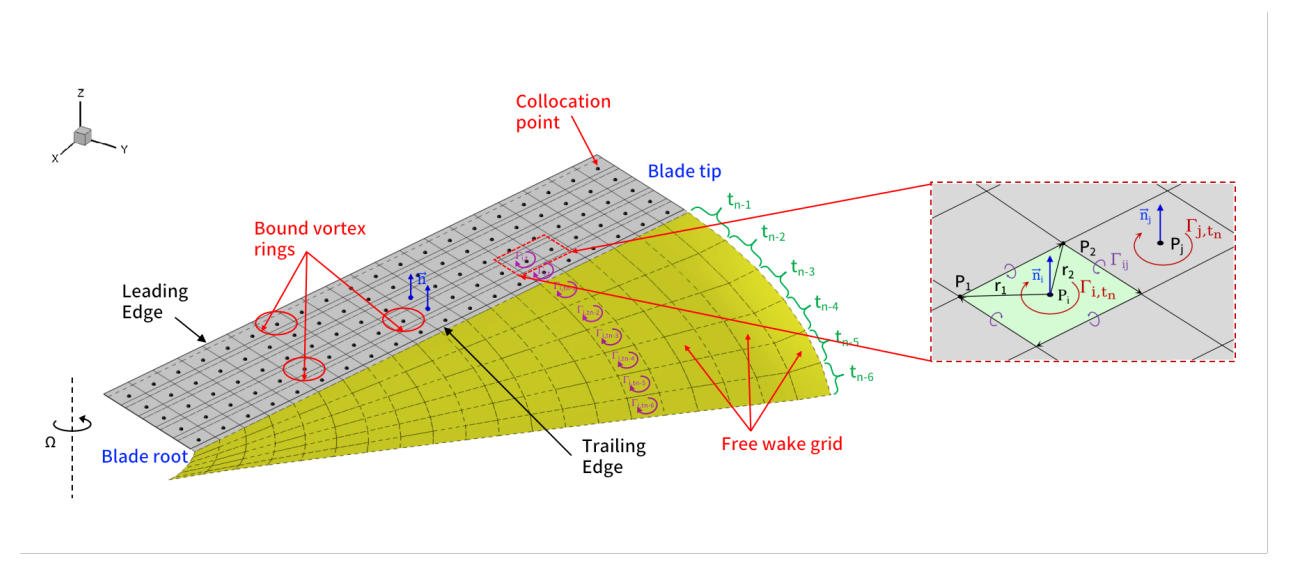


Fig. 1 Descriptive diagram of the Unsteady Vortex-Lattice Method (UVLM).

The induced velocity from each vortex ring element is computed using the Biot-Savart law and evaluated at the collocation point, located at the center of the three-quarter-chord line of each lifting surface panel. This treatment ensures that the vortex rings generate lift with a slope consistent with thin airfoil theory. The induced velocity is given by:

$$\mathbf{u}_{\text{ind}} = \frac{\Gamma}{4\pi} \frac{\mathbf{r}_1 \times \mathbf{r}_2}{|\mathbf{r}_1 \times \mathbf{r}_2|^2} \mathbf{r}_0 \cdot \left( \frac{\mathbf{r}_1}{|\mathbf{r}_1|} - \frac{\mathbf{r}_2}{|\mathbf{r}_2|} \right)$$
(4)

where  $\Gamma$  is the unknown vortex strength,  $\mathbf{r}_1$  and  $\mathbf{r}_2$  are vectors from the collocation point to the ends of the vortex

segment, and  $\mathbf{r}_0 = \mathbf{r}_1 - \mathbf{r}_2$  denotes the vortex segment vector.

To eliminate the singularities in the Biot-Savart equation during wake displacement in rotor simulations, the Vatistas vortex model [21] with n = 2 is employed. The modified induced velocity is defined as:

$$\mathbf{u}_{\text{ind}} = \frac{\Gamma}{4\pi} \frac{\mathbf{r}_1 \times \mathbf{r}_2}{\left(|\mathbf{r}_1 \times \mathbf{r}_2|^{2n} + |r_c \mathbf{r}_0|^{2n}\right)^{\frac{1}{n}}} \mathbf{r}_0 \cdot \left(\frac{\mathbf{r}_1}{|\mathbf{r}_1|} - \frac{\mathbf{r}_2}{|\mathbf{r}_2|}\right)$$
(5)

where  $r_c$  is the vortex core radius, typically set to 5% to 10% of the blade tip chord length. In the current work,  $r_c$  is adjusted using a viscous diffusion model to account for viscous effects:

$$r_c = \sqrt{r_{c_0}^2 + 4a\delta vt} \tag{6}$$

where  $r_{c_0}$  is the initial vortex core radius, set to 10% of the blade tip chord length, a = 1.25463 is the Oseen parameter from the Lamb-Oseen vortex model,  $\nu$  is the kinematic viscosity, and t is time. The average turbulent viscosity coefficient is  $\delta = 1 + a_1 Re_{\nu}$ , with the vortex Reynolds number defined as  $Re_{\nu} = \Gamma/\nu$ . The parameter  $a_1$  is set to  $O(10^{-2})$  for full-scale rotors and  $O(10^{-4})$  for small-scale rotors [15].

By applying the integral equation, Eq. (3), to each vortex ring element on lifting surfaces, the problem can be rewritten as a linear system:

$$[AIC]\Gamma = RHS \tag{7}$$

where [AIC] is the aerodynamic influence coefficient (AIC) matrix, and its element  $a_{ij}$  is defined as the velocity component induced by a unit strength of  $\Gamma_i$ , normal to the lifting surface at the collocation point i.

Once the vortex strength of each vortex ring element is determined, aerodynamic loads on the rotor blade are computed by integrating the UVLM solution with the viscous section data, taking advantage of the unsteady formulation of the Kutta-Joukowski theorem [22]:

$$\mathbf{F}_{i} = \rho_{\infty} \left( \Gamma_{i} - \Gamma_{i-1} \right) \mathbf{u}_{i} \times \mathbf{r}_{i} + \rho_{\infty} \frac{d\Gamma_{i}}{dt} A_{i} \mathbf{n}_{i}$$
(8)

where  $\mathbf{F}_i$  denotes the force on the vortex ring element i,  $\mathbf{r}_i$  is the vector of the first edge of the vortex ring, perpendicular to the freestream direction,  $\mathbf{u}_i$  is the velocity at the center of this edge,  $\mathbf{n}_i$  and  $A_i$  are the normal vector and area of the vortex ring, and  $\Gamma_i$  is the strength of the vortex ring element. In the first term,  $\Gamma_{i-1}$  is subtracted from  $\Gamma_i$ , the circulation strength of the preceding chordwise vortex ring panel, yielding the net circulation along  $\mathbf{r}_i$ . For the first panel in the chordwise direction, i.e., at the leading edge, the full circulation strength of the vortex ring element is used.

To include nonlinear effects, a low computational cost viscous-inviscid  $\alpha$ -iterative coupling algorithm is applied to each chordwise strip of vortex panels along the span of the blade. Each strip is corrected using a 2D viscous database

formatted as a .c81 table, which has been calculated with CHAMPS. The iterative viscous coupling algorithm is given as follows:

- 1) Solve the UVLM to obtain  $\Gamma$  and compute  $C_{L_{inv}}$  for every section
- 2) For every spanwise section, calculate the effective angle of attack  $\alpha_e$

$$\alpha_{\rm e} = \frac{{\rm C}_{\rm L_{inv}}}{2\pi} - \alpha_{\rm local} + \alpha_{\rm 3D}$$

- 3) Interpolate the  $C_{L_{vis}}$  from the 2D viscous database with  $\alpha_e$
- 4) Update the local angle of attack on the right-hand side of Eq. (7)

$$\alpha_{local} = \alpha_{local} + \varepsilon \left( \frac{C_{L_{vis}} - C_{L_{inv}}}{2\pi} \right)$$

where  $\varepsilon$  is a relaxation coefficient set at 0.2 in this work.

5) Repeat until the lift coefficient has converged for a given tolerance value

$$\|C_{L_{inv}} - C_{L_{vis}}\|_2 < 10^{-3}$$

# B. Vortex particle method (VPM)

The vortex particle method is a Lagrangian, grid-free approach that models the evolution of free wakes using viscous vortex particles to construct the vorticity field governed by the velocity-vorticity formulation of the incompressible Navier-Stokes equations:

$$\frac{D\omega}{Dt} = (\omega \cdot \nabla)\mathbf{u} + \nu \nabla^2 \omega \tag{9}$$

where  $\omega = \nabla \times \mathbf{u}$  is the vorticity field associated with the velocity field, and  $\nu$  is the kinematic viscosity of the flow. The first term on the right-hand side of Eq. (9) is the vortex stretching term that controls the stretching and deformation of the vortex, and the second term represents the viscous diffusion effects.

In VPM, the vorticity field can be expressed in a Lagrangian manner as the sum of the contributions of a set of  $N_p$  vector-valued particles,  $i_p$ :

$$\omega(\mathbf{x},t) = \sum_{i=1}^{N_p} \mathbf{\Gamma}_i(t) \zeta_{\sigma}(\mathbf{x} - \mathbf{x}_i(t))$$
(10)

where  $\mathbf{x}_i(t)$  and  $\mathbf{\Gamma}_i(t)$  are the position and vorticity intensity, respectively, of the *i*-th particle.  $\zeta_{\sigma}(\mathbf{x})$  is a smooth function, where  $\sigma$  is the smoothing radius that is greater than the distance between particles to guaranty the convergence

of VPM [23]. In this work, the 3D Gaussian distribution is adopted as the smooth function:

$$\zeta_{\sigma}(\rho) = \frac{1}{(2\pi\sigma^2)^{3/2}} e^{-\rho^2/2} \text{ and } \rho = \frac{|\mathbf{x} - \mathbf{x}_i(t)|}{\sigma}$$
(11)

the parameter  $\sigma$  is defined as the maximum distance from all neighboring particles in both streamwise and spanwise directions, and it remains constant throughout the simulation.

Based on Eq. (9), the evolution of viscous vortex particles can be represented by the system of ordinary differential equations in convection-diffusion form,

$$\frac{d\mathbf{x}_i(t)}{dt} = \mathbf{u}_i(t) \tag{12}$$

$$\frac{d\mathbf{\Gamma}_i(t)}{dt} = (\mathbf{\Gamma}_i(t) \cdot \nabla^{\mathrm{T}}) \mathbf{u}_i(t) + \nu \nabla^2 \mathbf{\Gamma}_i(t)$$
(13)

where  $i = 1, ..., N_p$ , for all particles. The first equation, which describes the convection of the *i*-th vortex particle transported by the local flow velocity, is adopted to update the particle positions. The second equation expresses the effect of vortex stretching and diffusion on the vorticity intensity of the *i*-th vortex particle, with the vortex stretching term in Eq. (13) employing a transposed scheme, as it provides the same information as the classical scheme while conserving total vorticity [24].

In the present work, the particle positions and the vorticity intensity are advanced in time using the low-storage 3<sup>rd</sup>-order Runge-Kutta scheme [25]. The particle-to-particle induced velocity can be approximated as:

$$\mathbf{u}_{i}(t) = -\sum_{i=1}^{N_{p}} \frac{1}{\sigma_{ij}^{3}} K(\rho) (\mathbf{x}_{i} - \mathbf{x}_{j}) \times \mathbf{\Gamma}_{j}$$
(14)

where  $K(\rho)$  is the Biot-Savart kernel for evaluating the particle-induced velocity.

$$K(\rho) = \frac{1}{\rho^2} \left[ \frac{1}{4\pi\rho} \operatorname{erf}\left(\frac{\rho}{\sqrt{2}}\right) - \frac{1}{(2\pi)^{3/2}} e^{\frac{-\rho^2}{2}} \right]$$
 (15)

then, the gradient of the particle-induced velocity in equation (14) can be expressed as

$$\nabla \mathbf{u}_i(t) = -\sum_{j=1}^{N_p} \nabla \left[ \frac{1}{\sigma^3} K(\rho) (\mathbf{x}_i - \mathbf{x}_j) \right] \times \mathbf{\Gamma}_j$$
 (16)

Eq. (14) and Eq. (16) can be computed using a direct method with a computational complexity of  $O(N^2)$ . However, these calculations become impractical when the number of particles is large. Therefore, a fast algorithm with lower

computational complexity is required. In this study, a Cartesian fast multipole method (FMM) is employed to accelerate these computations for vortex particles, reducing the numerical complexity from  $O(N^2)$  to O(N) [19].

The viscous diffusion term, which accounts for the effect of air viscosity on vorticity transportation, is solved using the PSE algorithm. This method approximates the Laplacian operator  $\nabla^2$  with an integral operator, thus avoiding direct numerical differentiation. Using this approach, the viscous diffusion effect from all shed vortex particles is expressed in a conservative form as

$$\frac{d\Gamma_i}{dt}|_{PSE} = \frac{2\nu}{\sigma^2} \sum_{j=1}^{N_p} \left( V_i \Gamma_j - V_j \Gamma_i \right) \zeta_{\sigma}(\rho)$$
(17)

To mitigate the instability of vortex stretching, which stems from inadequate compensation for viscous dissipation on subgrid scales due to the incomplete resolution of the full energy cascade, as described by Kolmogorov's theory [26], LES with an appropriate SGS model is employed. This approach allows for modeling eddies at smaller scales and capturing the coherent structures at coarser spatial resolutions than Direct Numerical Simulation (DNS). Therefore, Eq. (17) can be rewritten as a non-uniform viscosity distribution, as the SGS turbulent eddy viscosity introduces a spatially non-uniform viscosity field in LES.

$$\frac{d\alpha_i}{dt}|_{\text{PSE-LES}} = \frac{1}{\sigma^2} \sum_{i=1}^{N_p} \left( \nu_i + \nu_j \right) \left( V_i \mathbf{\Gamma}_j - V_j \mathbf{\Gamma}_i \right) \zeta_{\sigma}(\rho) \tag{18}$$

In this work, the standard Vreman SGS model [27] is adopted to calculate the eddy viscosity in LES, owing to its superior transitional and near-wall performance, as well as its robustness in high Reynolds number flows compared to the standard Smagorinsky SGS model [27]. The eddy viscosity in the Vreman model is expressed as:

$$v_{\text{tur}} = c_V \sqrt{\frac{\Pi_\beta}{\alpha_{ij}\alpha_{ij}}} \text{ and } \alpha_{ij} = \frac{\partial u_j}{\partial x_i}$$
 (19)

$$\Pi_{\beta} = \beta_{11}\beta_{22} - \beta_{12}^2 + \beta_{11}\beta_{33} - \beta_{13}^2 + \beta_{22}\beta_{33} - \beta_{23}^2 \text{ and } \beta_{ij} = \sum_{m=1}^3 \Delta_m^2 \alpha_{mi} \alpha_{mj}$$
 (20)

where  $c_V$  is the model coefficient, related to the standard Smagorinsky constant  $c_S$  by  $c_V \approx 2.5c_S^2$ . In this study,  $c_V$  is set to 0.07.  $\Delta_m$  denotes the filter width at the particle level in the *m*-th direction, typically set to the particle core size  $\sigma$ .

Fig. 2 presents a DJI Phantom II rotor wake from the current VPM simulation at an advance ratio of J = 0.35. The simulation is able to capture every stage of the wake, from a coherent vortex structure to turbulent breakdown and mixing, and it predicts transitional mechanisms in between, such as short-wave instability, leapfrog, and pairing.

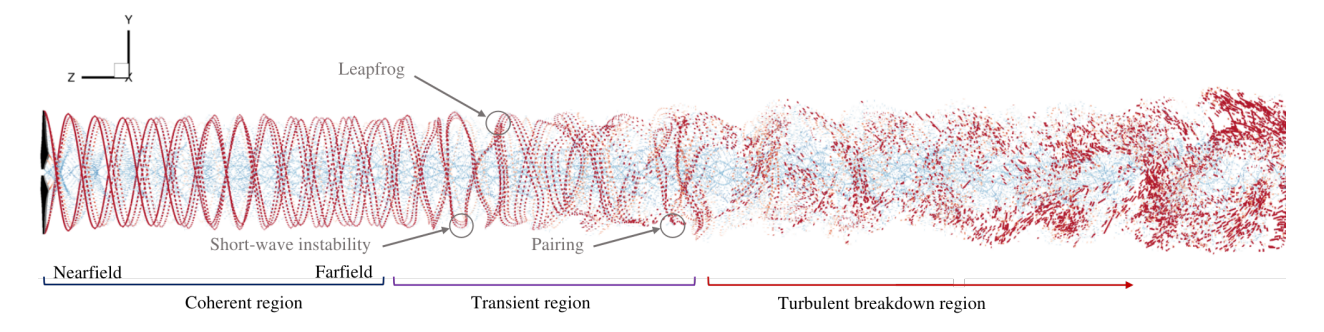


Fig. 2 The current VPM simulation capturing the wake evolution of a DJI Phantom II rotor at J = 0.35 from a coherent vortical structure to turbulent breakdown and mixing.

# C. Coupling strategy

To address the singularity and stretching issues in wake panels, vortex ring elements in the wake can be replaced with vortex particles. Following this approach, the wake shed from the blade trailing edge is initially represented as straight-line vortex elements, with the strength of upstream vortex lines remaining unchanged to prevent circulation strength discontinuity at the trailing edge. These wake panels are then converted into vortex particles after a prescribed number of time steps, as illustrated in Fig. 3. Here, the streamwise particles (shown in green) represent trailed particles, and the spanwise particles (shown in red) are shed particles. The strength of each new particle is proportional to the circulation difference between two adjacent wake panels, as given by:

$$\Gamma_i = \frac{\Delta \Gamma d\mathbf{l}}{n_i} \tag{21}$$

where  $d\mathbf{l}$  is the vector length of the straight-line vortex element,  $\Delta\Gamma$  represents the circulation difference between two wake panels on either side of the edge, and  $n_i$  is the number of particles approximating the i-th straight-line element.

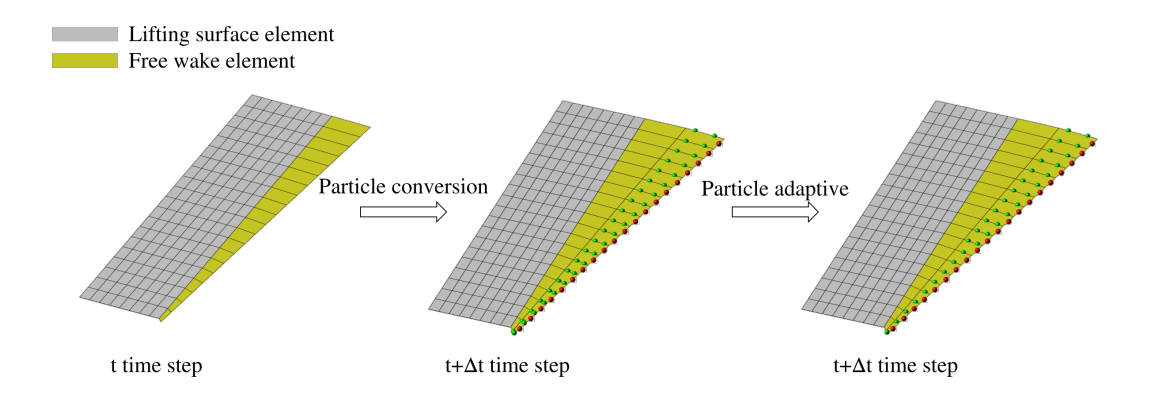


Fig. 3 The conversion of wake panels to particles.

In rotor simulations, the streamwise length of trailing vortex segments increases with radial position, resulting in significant variations along the blade span. If each trailing segment is converted into the same number of vortex particles, the particle distribution becomes highly non-uniform in space, causing inefficient use of computational resources and reduced performance, particularly in multi-rotor simulations. To address this issue, an adaptive approach is employed in which the number of vortex particles assigned to each trailing vortex segment is scaled according to its radial length, based on the prescribed particle count at the blade tip vortex segment, as shown in Fig. 3.

Let  $\Delta s_t$  represent the streamwise length of the blade tip vortex segment, with a prescribed number of vortex particles  $n_t$ . The number of vortex particles  $n_i$  for each trailing vortex segment with streamwise length  $\Delta s_i$  can be calculated as:

$$n_i = \left\lceil \frac{\Delta s_i \cdot n_t}{\Delta s_t} \right\rceil \tag{22}$$

where  $\lceil \cdot \rceil$  denotes upward rounding. The effectiveness assessment of this adaptive approach is discussed in Sec. III.A.

# D. Multiple reference frames

In helicopter rotor systems, each blade is typically connected to the rotor hub through a set of hinges, allowing independent blade motion. Although rotor blades are inherently highly elastic, this work simplifies the analysis by considering the blades to be rigid, with the implications of this assumption acknowledged. Under this simplification, the rigid blades can move relative to the hinge positions. The descriptions of these hinges are as follows: (1) the pitch hinge allows blade rotation about the 1/4-chord and spanwise axis; (2) the flap hinge enables blade motion within the plane defined by the blade and the shaft; (3) the lead-lag hinge allows blade motion in-plane, forward and backward. The blade pitching  $\theta$ , flapping  $\beta$ , and lead-lag  $\delta$  motion can then be expressed by the Fourier series as a function of the azimuth angle  $\psi$ :

$$\psi = \omega t$$

$$\theta(\psi) = \theta_0 + \theta_{1c} \cos(\psi) + \theta_{1s} \sin(\psi) + \theta_{2c} \cos(2\psi) + \theta_{2s} \sin(2\psi) + \cdots$$

$$\beta(\psi) = \beta_0 + \beta_{1c} \cos(\psi) + \beta_{1s} \sin(\psi) + \beta_{2c} \cos(2\psi) + \beta_{2s} \sin(2\psi) + \cdots$$

$$\delta(\psi) = \delta_0 + \delta_{1c} \cos(\psi) + \delta_{1s} \sin(\psi) + \delta_{2c} \cos(2\psi) + \delta_{2s} \sin(2\psi) + \cdots$$
(23)

where  $\omega$  is the constant angular velocity of the rotor system about the z-axis,  $\theta_0$  is the collective pitch angle, and  $\beta_0$  is the pre-cone angle. The lateral and longitudinal components of the motion are represented by subscripts c and s, respectively. In this work, only the first harmonic term is considered.

In the present model, the blade Cartesian coordinates are sequentially transformed from the ground reference frame to the helicopter body frame and then to the rotor hub frame using a series of rotation matrices. Finally, the hub frame is mapped to each blade's local reference frame, where the motion laws defined in Eq. (23) are applied. Based on the complete definition of the reference system illustrated in Fig. 4, the blade motion can be described through a hierarchy of coordinate transformations. Starting from the ground reference frame, the helicopter body rotates around the z-, y-, and x-axes with yaw ( $\Psi$ ), pitch ( $\Theta$ ), and roll ( $\Phi$ ) angles, respectively. The transformation from the body frame to the rotor hub frame introduces the shaft tilt angle  $\alpha_s$ , which represents the inclination of the rotor shaft relative to the fuselage and is typically defined as a rotation around the body y-axis. The subsequent transformation to the rotor frame accounts for the azimuthal rotation  $\psi$  about the z-axis, followed by the flapping  $\beta$  around the x-axis, the leading motion  $\delta$  around the z-axis, and the pitching movement  $\theta$  around the y-axis. The corresponding transformation matrices are then defined to prescribe the complete kinematics of the rotor blade.

$$C_{GH}(\Phi,\Theta,\Psi) = \begin{pmatrix} \cos\Psi\cos\Theta & \cos\Psi\sin\Theta\sin\Phi - \sin\Psi\cos\Phi & \cos\Psi\sin\Theta\cos\Phi + \sin\Psi\sin\Phi\\ \sin\Psi\cos\Theta & \sin\Psi\sin\Theta\sin\Phi + \cos\Psi\cos\Phi & \sin\Psi\sin\Theta\cos\Phi - \cos\Psi\sin\Phi\\ -\sin\Theta & \cos\Theta\sin\Phi & \cos\Theta\cos\Phi \end{pmatrix},$$

$$C_{HR}(\alpha_s) = \begin{pmatrix} \cos \alpha_s & 0 & -\sin \alpha_s \\ 0 & 1 & 0 \\ \sin \alpha_s & 0 & \cos \alpha_s \end{pmatrix}, \quad C_{RF}(\psi) = \begin{pmatrix} \cos \psi & -\sin \psi & 0 \\ \sin \psi & \cos \psi & 0 \\ 0 & 0 & 1 \end{pmatrix}, \tag{24}$$

$$C_{FL}(\beta) = \begin{pmatrix} 1 & 0 & 0 \\ 0 & \cos\beta & -\sin\beta \\ 0 & \sin\beta & \cos\beta \end{pmatrix}, \qquad C_{LP}(\delta) = \begin{pmatrix} \cos\delta & -\sin\delta & 0 \\ \sin\delta & \cos\delta & 0 \\ 0 & 0 & 1 \end{pmatrix}, \qquad C_{PB}(\theta) = \begin{pmatrix} \cos\theta & 0 & -\sin\theta \\ 0 & 1 & 0 \\ \sin\theta & 0 & \cos\theta \end{pmatrix}$$

where  $C_{PB}$ ,  $C_{LP}$ ,  $C_{FL}$ ,  $C_{RF}$ ,  $C_{HR}$ , and  $C_{GH}$  represent the linear transformation matrices for blade pitching, blade lead-lag, blade flapping, rotor rotation, rotor shaft, and helicopter movement, respectively. Then, the coordinates  $\mathbf{x}_p$  and velocity vector  $\mathbf{u}_p$  of a point p in the ground reference frame (GF) become the following:

$$[\mathbf{x}_{p}]_{RF} = C_{RF}(\psi) \cdot (C_{FL}(\beta) \cdot (C_{LP}(\delta) \cdot (C_{PB}(\theta) \cdot [\mathbf{x}_{0}]_{BF} + \mathbf{H}_{P}) + \mathbf{H}_{L}) + \mathbf{H}_{F})$$

$$[\mathbf{x}_{p}]_{GF} = \mathbf{V}_{\infty}t + C_{GH}(\Phi, \Theta, \Psi) \cdot C_{HR}(\alpha_{s}) \cdot [\mathbf{x}_{p}]_{RF}$$

$$[\mathbf{u}_{p}]_{GF} = \frac{d[\mathbf{x}_{p}]_{GF}}{dt}$$
(25)

where  $\mathbf{H}_{P}$ ,  $\mathbf{H}_{L}$ , and  $\mathbf{H}_{F}$  define the lengths of the pitch hinge, lead-lag hinge, and flap hinge, respectively.

#### E. RANS solver – CHAMPS (CHApel Multi-Physics Simulation)

CHAMPS (CHApel Multi-Physics Simulation) is an in-house software developed at Polytechnique Montréal for aerodynamic, aeroelastic, and aeroicing simulations [18]. It implements classic compressible RANS-based algorithms in the Chapel language, serving as an alternative to MPI libraries for distributed memory parallelism. The solver has been verified and validated on NASA test cases, including the flat plate, NACA 0012, and others [28]. In this study, aerodynamic simulations for 2D airfoils were conducted using a cell-centered, unstructured finite volume method. A

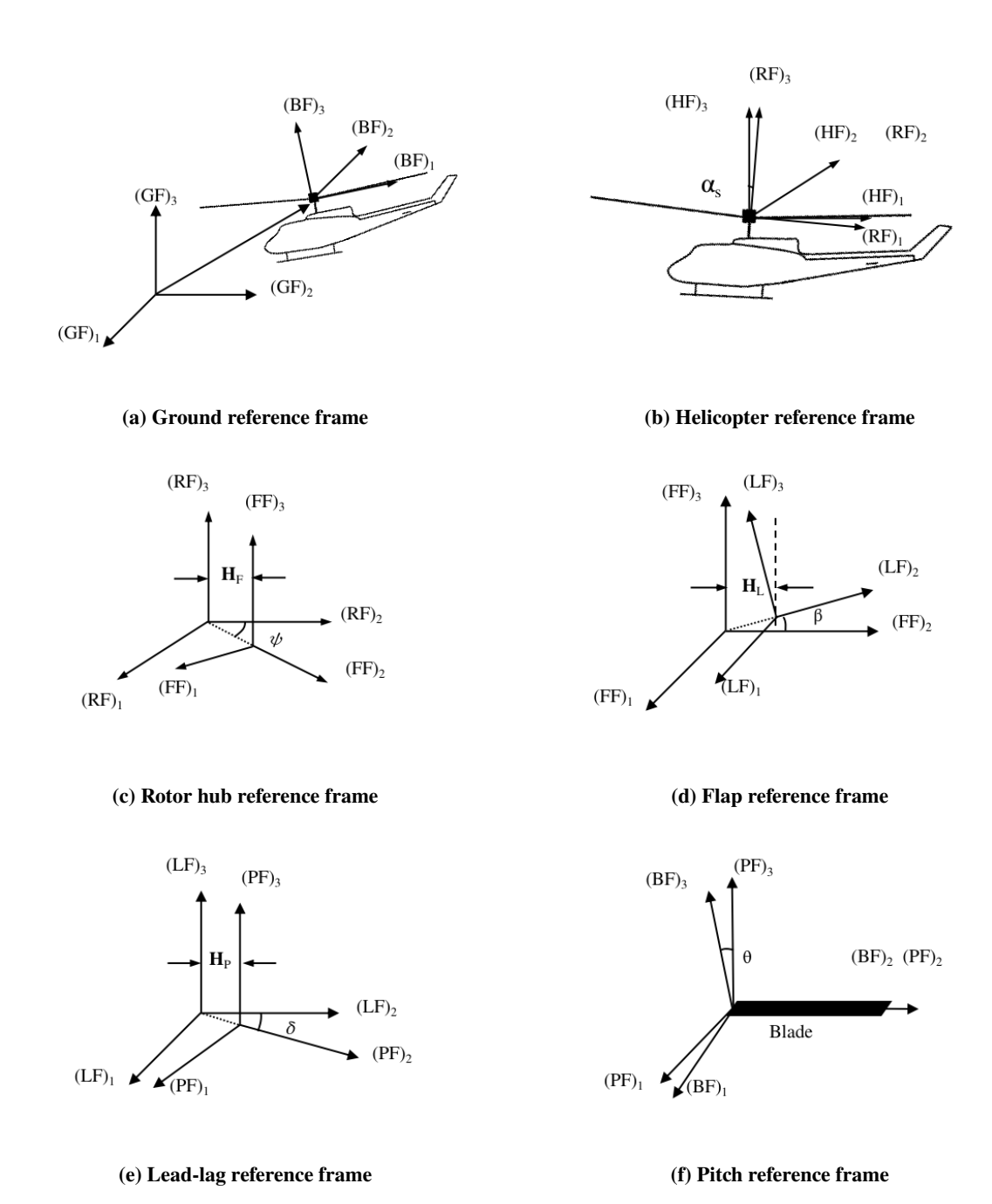


Fig. 4 Schematic of multiple reference frames for helicopter.

second-order Roe scheme with piecewise linear reconstruction was employed to discretize the convective fluxes of the RANS equations. Gradients were computed using the weighted least squares approach with the Venkatakrishnan limiter. For all cases, the standard one-equation Spalart-Allmaras (SA) turbulence model was adopted, with its convective fluxes discretized using a first-order upwind scheme. The RANS equations and turbulence model were solved separately in a segregated approach, both iterated in pseudo-time using an implicit Euler scheme, with the linear systems solved through

a Block Symmetric Gauss-Seidel (BSGS) method. Convergence of all simulations was achieved with a reduction of six orders of magnitude in the L2-norm of the density residual.

An O-mesh topology was employed, with outer boundaries positioned 60 chord lengths away, to compute the airfoil aerodynamics over an angle of attack (AOA) range from  $-180^{\circ}$  to  $180^{\circ}$ . A mesh independence study was conducted using cell densities of  $128 \times 72$ ,  $256 \times 144$ , and  $512 \times 288$  to evaluate the impact of grid resolution on aerodynamic predictions. This study included a comparison of lift and drag coefficients for the symmetric NACA0012 airfoil at  $\alpha = 4^{\circ}$ , M = 0.4, and  $Re = 2 \times 10^{6}$ . Table 2 demonstrated that the  $256 \times 144$  mesh is sufficient for achieving grid-independent solutions from an engineering perspective. Therefore, it is suitable for generating a further airfoil aerodynamic database to ensure precision and efficiency simultaneously.

Table 2 Grid independence study

	_	•
Mesh dimension	$C_L$	$C_D$
$128 \times 72$	0.46704	0.014291
$256 \times 144$	0.47488	0.012180
$512 \times 288$	0.47578	0.011513

# F. URANS solver – ROSITA (ROtorcraft Software ITAly)

The high-fidelity URANS results for rotor flow simulations are provided by ROSITA (ROtorcraft Software ITAly) [29], an MPI-parallel, overset, multi-block, structured grid solver of the RANS equations coupled with the SA turbulence model. The governing equations are spatially discretized using a cell-centered finite volume implementation of Roe's approximate Riemann solver [30]. Second-order accuracy is achieved through the Monotone Upstream-centered Schemes for Conservation Laws (MUSCL) extrapolation, supplemented with a modified version of the Van Albada limiter introduced by Venkatakrishnan [31]. Viscous fluxes are evaluated using Gauss's theorem and a cell-centered discretization scheme. Temporal integration is performed through a dual-time-stepping formulation employing a second-order backward differentiation for the physical time derivative and a fully unfactored implicit scheme for pseudo-time advancement. The resulting linear system is solved using a generalized conjugate gradient (CGC) method in conjunction with a block incomplete lower-upper (BILU) preconditioner. The overset grid system is connected via the CHIMERA technique, based on the modified Chesshire and Henshaw algorithm [32], while the Octree and alternating digital tree data structures are adopted to speed up the cell-tagging and hole-cutting processes.

#### III. Results and Discussion

The following section presents and discusses the results obtained using the NL-UVLM-VPM method for helicopter rotor flows. The analysis starts with an evaluation of the adaptive panel-to-particle conversion approach and the determination of an appropriate temporal discretization for rotor wake simulations, as detailed in Sec. III.A. Subsequently,

three benchmark cases are employed to validate the NL-UVLM-VPM method. Comparisons between the NL-UVLM-VPM predictions and experimental or URANS data are conducted to validate the proposed solver in capturing critical aerodynamic characteristics in typical rotor scenarios. The first validation case, presented in Sec. III.B, considers the two-bladed Caradonna-Tung rotor tested in the US Army Aeromechanics Laboratory's hover test facility [33]. The classic configuration serves as a fundamental benchmark to assess the method's ability to predict hovering rotor performance. Then, the full-scale AH-1G main rotor, for which a flight test was conducted by researchers at the US Ames Research Center [34], is employed as a forward flight benchmark that includes pronounced BVI phenomena. This case allows for the evaluation of the solver in capturing unsteady aerodynamic loads and wake dynamics. The results will be presented in Sec. III.C. Finally, Sec. III.D investigates a more complex configuration involving large-scale, side-by-side helicopter rotor models [35]. This case is selected to assess the capability of the NL-UVLM-VPM framework in reproducing rotor-rotor aerodynamic interference effects and the resulting induced flow changes between interacting rotors.

#### A. Adaptive panel-particle conversion assessment

To assess the adaptive panel-particle conversion approach associated with the rotor simulation, Fig. 5 presents the spatial distribution of particles shed from the trailing edge after  $10^{\circ}$  azimuthal angle for four rotor wake shedding cases. It is seen that as  $\Delta\psi$  increases from  $2.5^{\circ}$  to  $5.0^{\circ}$  while maintaining a single particle per trailing segment ( $n_t = 1$ ), the wake resolution becomes significantly coarser, particularly near the blade tip. Increasing  $n_t$  to 2 improves the near-tip resolution but still leads to uneven spacing along the span. In contrast, the adaptive scheme automatically scales the number of particles per segment with the local streamwise length, producing a more uniform particle distribution and a smoother wake geometry across the entire span.

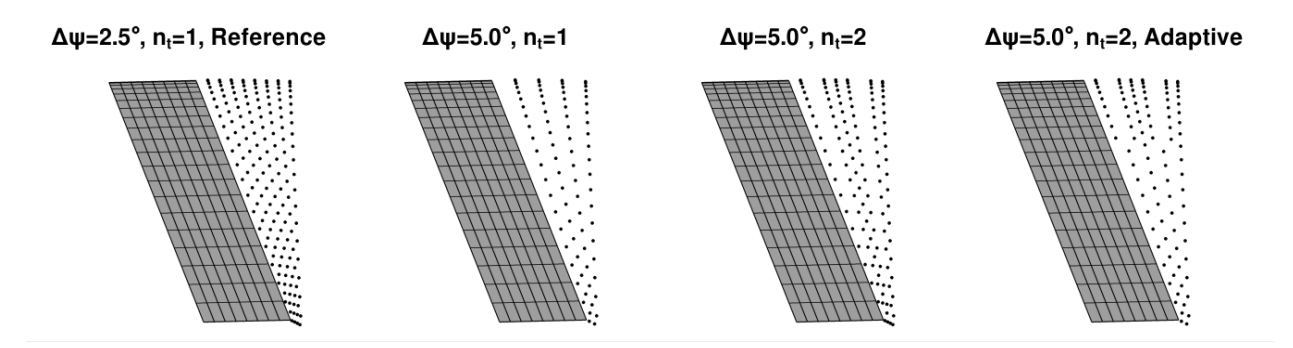


Fig. 5 Comparison of four rotor wake shedding cases after 10° azimuthal angle.

For NL-UVLM-VPM calculations on a hovering rotor, the impulsive rotation method induces nonphysical instability in the initial wake and occasionally causes the entire simulation to fail. This issue arises due to a strong upward velocity at the blade root compared to the downward velocity. To overcome these nonphysical effects, a slow rotation method, which gradually increases the rotation speed from zero to the target, is adopted [36]. As described in Eq. (26), the

angular velocity  $(\Omega_s)$  of the rotor is increased linearly over an initial number of revolutions  $(N_s)$ , reaching the target velocity  $(\Omega_t)$ .

$$\Omega_{\rm s} = \Omega_{\rm t} \frac{N_{\rm rev}}{N_{\rm s}} \tag{26}$$

In the present computation, a slow-start procedure with  $N_s=3$  is applied to mitigate initial wake instability. Fig. 6 shows the convergence histories of the thrust and torque coefficients. As seen in the insets, the adaptive approach achieves nearly identical values to the reference case ( $\Delta\psi=2.5^{\circ}$  and  $n_t=1$ ), indicating that the adaptive method maintains numerical accuracy even when the time-step size is coarser.

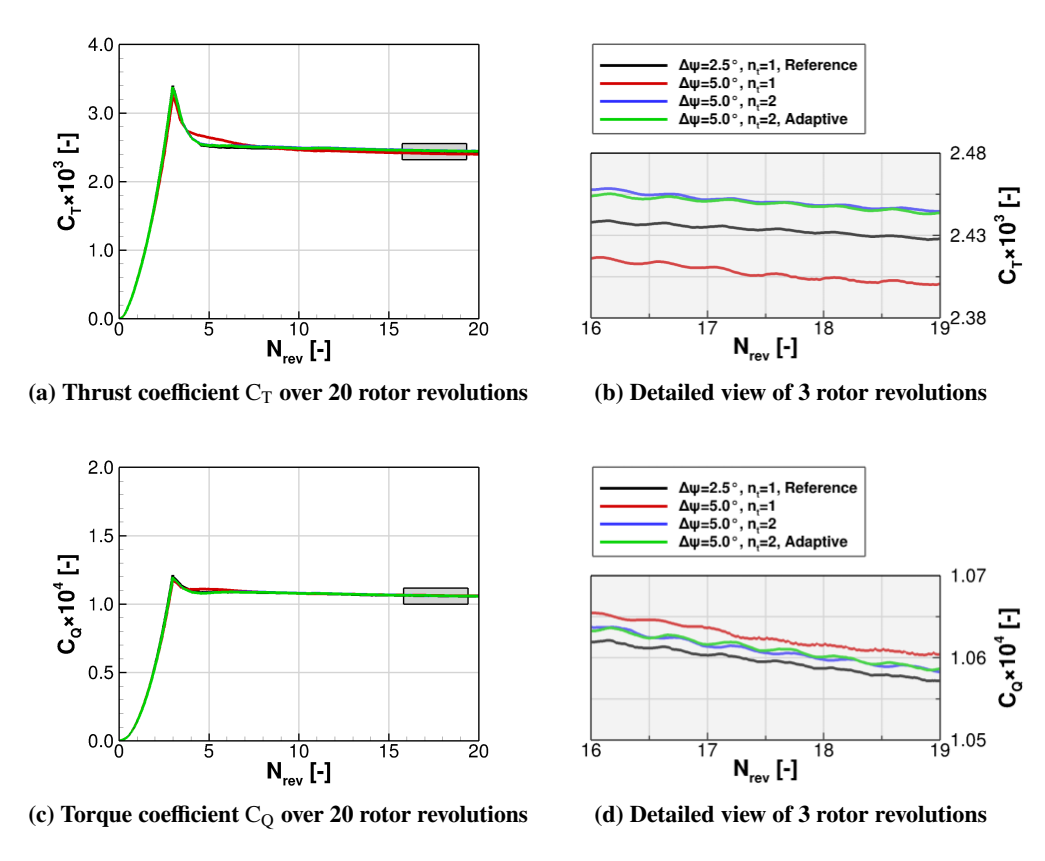


Fig. 6 Convergence history of the overall thrust and torque coefficients.

A quantitative comparison is then provided in Table 3. Computations were conducted on a single AMD EPYC 9655 (Zen 5)@2.6 GHz processor with 96 cores and 192 threads. Compared to the reference case, the adaptive case reduces the total number of particles by approximately 38% and saves the computational wall-time by nearly 70%, while keeping the deviations in  $C_T$  and  $C_Q$  within 1.0%. These results confirm that the adaptive particle conversion significantly improves computational efficiency without compromising numerical stability or accuracy.

To further verify the physical consistency of the adaptive approach, Fig. 7 displays the instantaneous wake structures obtained with different discretization strategies after 20 rotor revolutions in a hovering condition, where the colors are

Table 3 Adaptive conversion assessment of rotor wake shedding cases

Case	C <sub>T</sub> deviation	C <sub>Q</sub> deviation	Number of particles	CPU wall-time
$\Delta \psi = 2.5^{\circ}, n_t = 1, \text{Reference}$			235996	8.0 h
$\Delta \psi = 5.0^{\circ}, n_{\rm t} = 1$	-1.2%	+0.31%	117916	2.0 h
$\Delta \psi = 5.0^{\circ}, n_{\rm t} = 2$	+0.7%	+0.09%	178312	3.5 h
$\Delta \psi = 5.0^{\circ}, n_t = 2, Adaptive$	+0.6%	+0.09%	146676	2.5 h

rendered by the intensity of turbulent viscosity  $v_t$ . In the reference case ( $\Delta \psi = 2.5^{\circ}$ ,  $n_t = 1$ ), the wake maintains a well-organized helical structure, with clearly defined tip vortices and significant contraction near the rotor disk plane. Additionally, the progressive increase of  $v_t$  downstream reflects a smooth transition from the coherent region to the onset of turbulence. When the azimuthal step is doubled to  $\Delta \psi = 5.0^{\circ}$  while keeping  $n_t = 1$ , the near-disk region exhibits higher values of the  $v_t$  than in other cases, and the transitional region is nearly absent. This behavior arises from the insufficient temporal and spatial resolution associated with the larger time step. Each trailing vortex segment is stretched over a long distance before being discretized into particles, resulting in coarser particle spacing and an under-resolved shear layer at the blade tip. As a result, the subgrid-scale model is prematurely activated, producing excessive numerical diffusion that suppresses the natural instability growth responsible for the coherent-to-turbulent transition. Increasing the number of particles per trailing segment to  $n_t = 2$  alleviates part of this issue by improving the local resolution of the vortex filaments, which allows the transitional region to reappear further downstream. However, mild over-diffusion still occurs in the near wake due to the uniform distribution of particles along the span. In contrast, the adaptive method with  $\Delta \psi = 5.0^{\circ}$  and  $n_t = 2$  maintains a consistent spatial resolution throughout the entire wake, thereby preserving the physically consistent evolution of the wake and producing the overall wake topology and turbulence evolution with good agreement with the reference case, despite slight discrepancies that are still observed in the far-field of the wake. This represents a practical trade-off between accuracy and efficiency for rotor wake simulations.

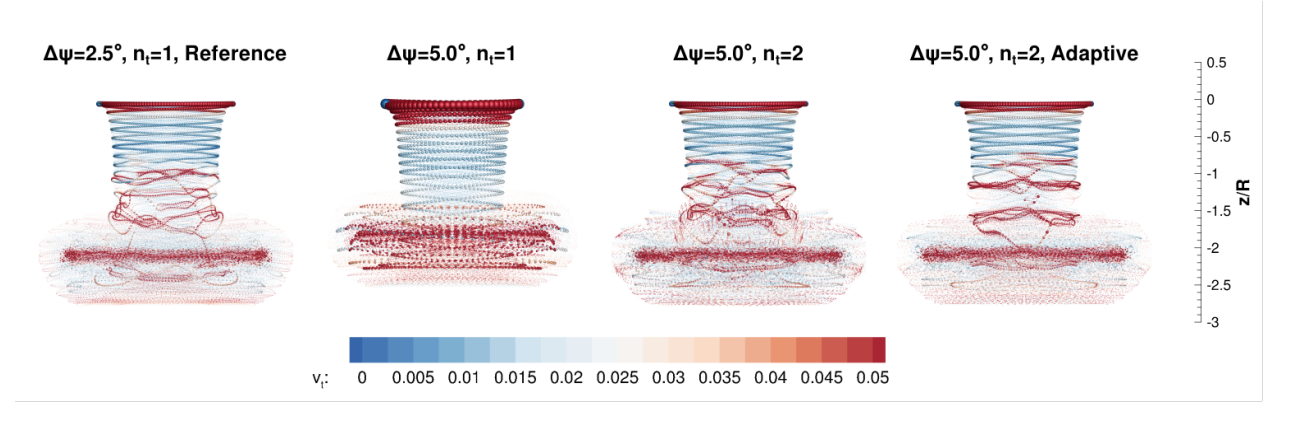


Fig. 7 Instantaneous wake structures after 20 rotor revolutions for different discretization strategies, colored by turbulent viscosity  $\nu_t$ .

Overall, this adaptive approach optimizes computational resource efficiency while maintaining accuracy and ensuring

spatial discretization consistency between the UVLM and the VPM. Furthermore, this treatment enables the maintenance of equivalent time accuracy with a larger azimuthal time step compared to a smaller one. Building on this,  $\Delta \psi = 5.0^{\circ}$  and  $n_t = 2$  with the adaptive approach are employed in the subsequent applications.

#### B. Hovering case: Caradonna-Tung rotor

The well-known Caradonna and Tung (C-T) hovering rotor case [33] is adopted to assess the mid-fidelity computational tool. The two-bladed C-T rotor has rectangular, untwisted blades with an aspect ratio of 6. The blade profile consists of a symmetric NACA0012 airfoil with a chord length of 0.1905 m. The rotor has a radius of 1.143 m and a pre-cone angle of 0.5°. The operational conditions considered in this study are reported in Table. 4.

Table 4 Hover test conditions for C-T rotor[33]

Collective pitch $(\theta_c)$	Blade Tip Mach number (M <sub>T</sub> )	
5°		
8°	0.439	
12°		

The high-fidelity URANS simulations for the C-T rotor in hover employed a time-accurate approach. A Chimera grid system with 8.65 million cells was used to facilitate the movement of the rotor blade mesh over the background mesh. Fu et al. [37] performed a grid convergence study using the ROSITA solver, considering a range of grid resolutions from coarse to fine. Grid independence was verified by monitoring the blade pressure distribution, with the medium resolution grid providing satisfactory accuracy within a reasonable time cost. In the present work, the same medium resolution grid and solver numerical setup are applied to generate high-fidelity simulation results instead of repeating the grid convergence study. Due to the high computational effort required for the time-accurate approach, the simulation took approximately 3.3 days to complete 5 rotor revolutions, with each revolution requiring about 16 hours using the URANS solver running in parallel on 240 processors.

In NL-UVLM-VPM simulations, the blade discretization parameters are selected based on grid-dependence studies conducted in previous work [19], which determined that an  $8 \times 20$  panel layout (uniform chordwise and sine spanwise spacing) provides an appropriate compromise between accuracy and computational efficiency. Meanwhile, the total number of rotor revolutions is 20, including three slow startup revolutions ( $N_s = 3$ ) to eliminate wake instability.

Figure 8 provides a comparison among experimental data, URANS results, and the NL-UVLM-VPM predictions of the integrated thrust coefficient for various collective pitch angles. All simulations overestimate the measurements, with smaller differences observed between NL-UVLM-VPM results and measured data than those with URANS.

The chordwise pressure coefficient ( $C_P$ ) distributions at radial positions of r/R = 0.68, 0.80, and 0.89 for the test condition of  $\theta_c = 5^\circ$  are shown in Fig. 9. In the NL-UVLM-VPM framework, the pressure coefficient is reconstructed by interpolating the sectional  $C_P$  values obtained from the 2D RANS database based on the effective angle of attack for each

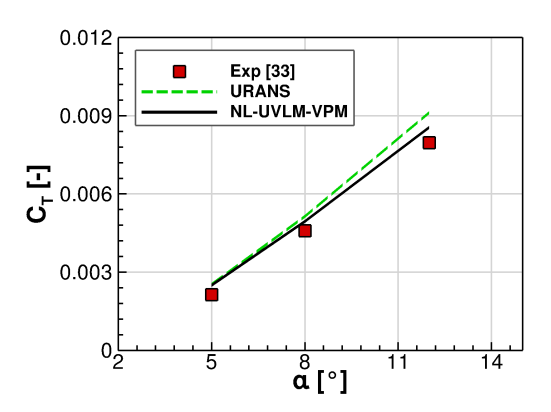


Fig. 8 Comparison of integrated rotor thrust coefficient on various collective pitch angles.

blade section. It can be seen that the present numerical results are in fairly good agreement with both the experimental measurements and high-fidelity URANS results for all radial positions. However, minor discrepancies become more significant toward the blade tip, primarily due to stronger three-dimensional effects and tip-vortex influence.

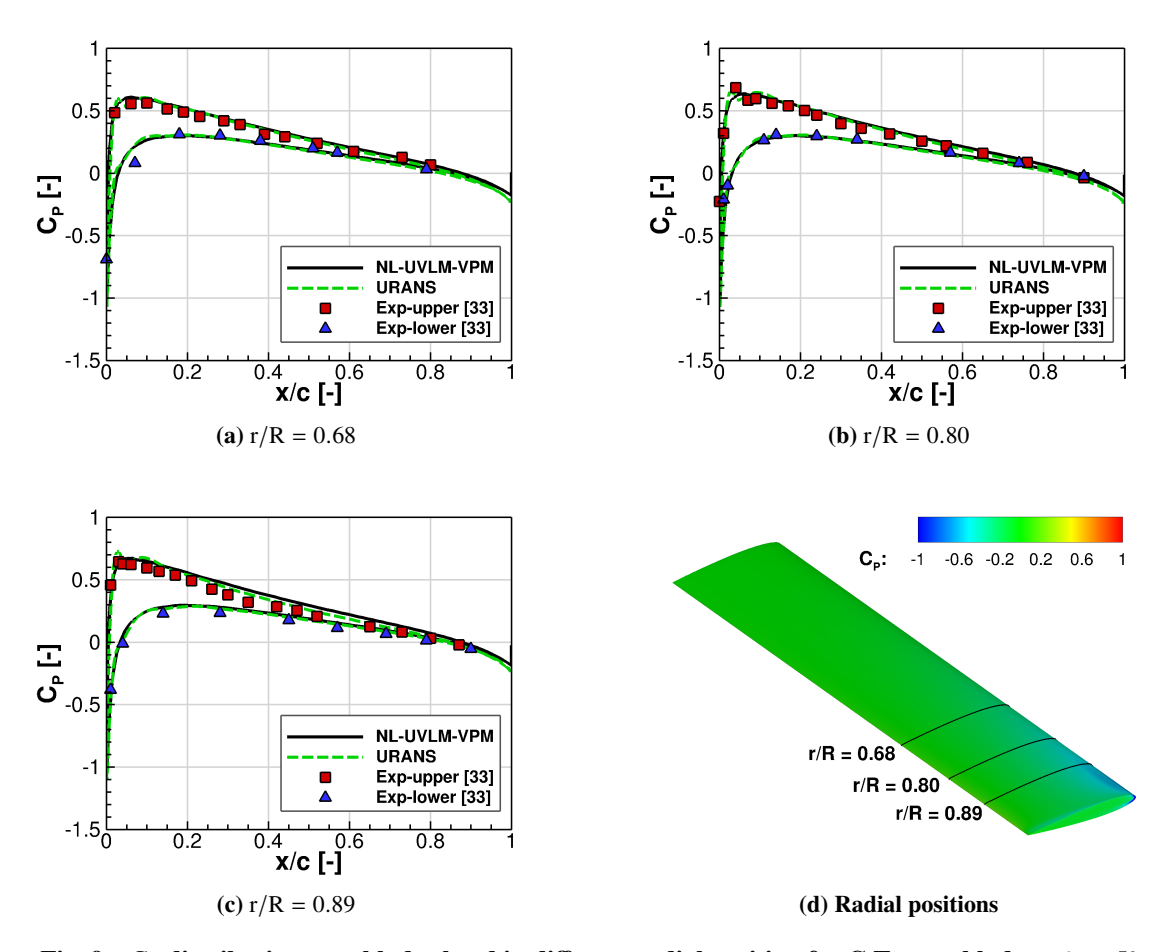


Fig. 9  $C_P$  distribution over blade chord in different radial position for C-T rotor blade at  $\theta_c = 5^\circ$ .

Fig. 10 compares the predicted tip vortex trajectories with experimental measurements and high-fidelity URANS results at three collective pitch angles:  $\theta_c = 5^\circ$ ,  $8^\circ$ , and  $12^\circ$ . The trajectories are represented in terms of the normalized radial (r/R) and axial (-z/R) positions as functions of vortex age. For all pitch settings, the NL-UVLM-VPM results show reasonable agreement with both experimental data and URANS predictions, reproducing the radial contraction and axial convection of the tip vortex. At  $\theta_c = 5^\circ$ , the predicted contraction rate agrees well with both URANS and the experiment, whereas the axial descent rate is slower than the experiment but follows the experimental trend more closely than the URANS prediction. When the pitch increases to  $\theta_c = 8^\circ$ , the URANS results present a steeper vortex descent and a stronger contraction relative to the experiment, while the NL-UVLM-VPM prediction not only reproduces this trend but also exhibits better agreement with the measurements. At the maximum pitch setting of  $\theta_c = 12^\circ$ , both URANS and NL-UVLM-VPM approaches capture pronounced downward convection and tighter wake contraction, consistent with the increased induced velocity and thrust load. Simultaneously, it is observed that the discrepancy between predicted and measured trajectories becomes more significant as the collective pitch increases, reflecting the high sensitivity of the wake geometry to the induced velocity field at large thrust loads. Overall, the comparative data demonstrate that the present NL-UVLM-VPM approach reliably resolves the near-wake geometry.

#### C. Forward flight case: AH-1G main rotor

This section compares the mid-fidelity simulation results for the AH-1G main rotor with flight test data from [34] and high-fidelity URANS data under forward flight conditions.

The AH-1G main rotor comprises two rectangular, untapered blades with a linear distribution, using a symmetric airfoil from the Operational Load Survey/Tip Aerodynamics and Acoustics Test (OLS/TAAT). The geometric properties of the AH-1G main rotor are summarized in Table. 5. The blade motion given by the experiment is expressed as follows:

Table 5 Geometric properties [34]

Given value
2
Rectangular
OLS/TAAT
6.7 m
0.7283 m
Linear, $-10.0^{\circ}$
0.154R

$$\theta(\psi) = 6.0 + 1.7\cos(\psi) - 5.5\sin(\psi)$$

$$\beta(\psi) = 2.13\cos(\psi) - 0.15\sin(\psi)$$
(27)

The low-speed case corresponding to test point 2157 was used for this study. The rotor operated at an advance ratio of 0.19 and a blade tip Mach number of 0.65, with both pre-cone and shaft angles set to  $0.0^{\circ}$ .

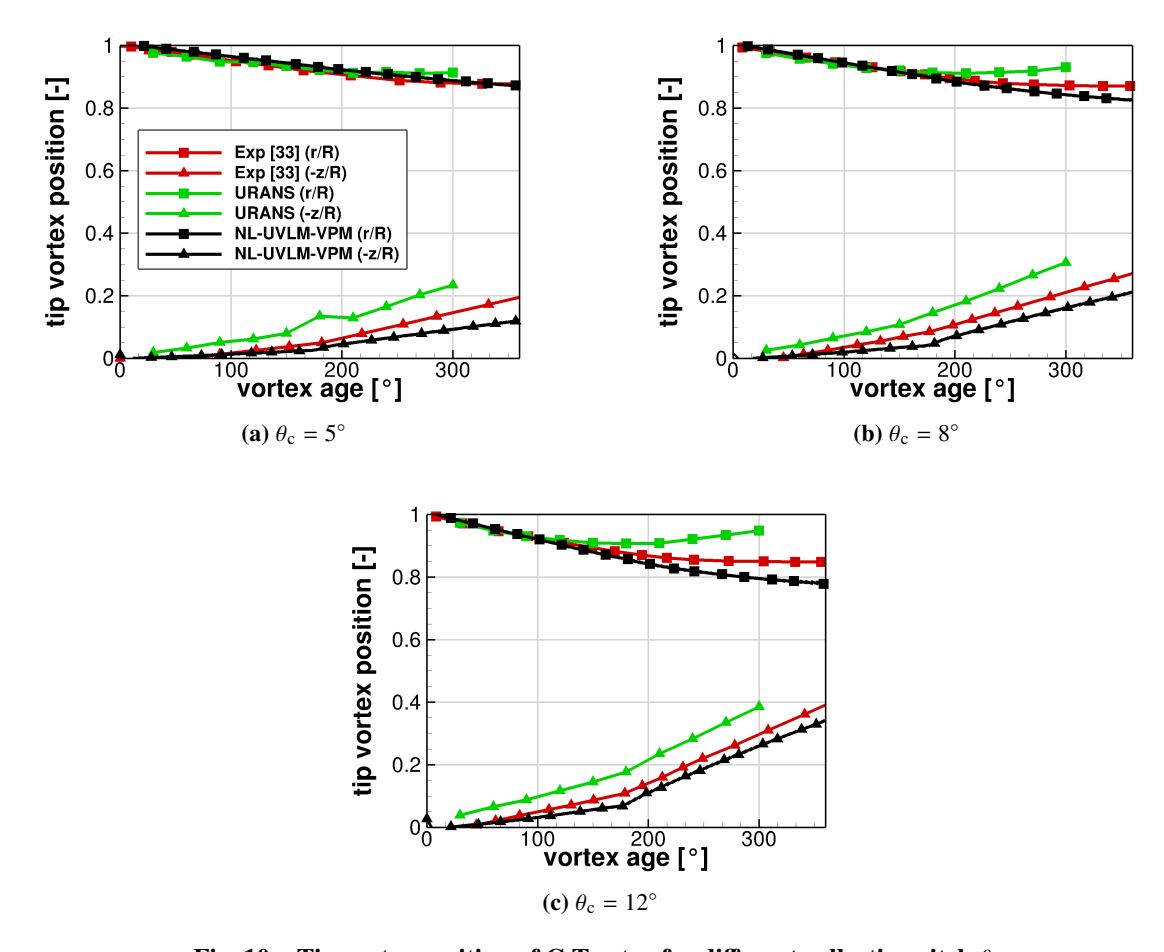


Fig. 10 Tip vortex position of C-T rotor for different collective pitch  $\theta_c$ .

High-fidelity URANS computation of the AH-1G main rotor was performed using the ROSITA solver in an unsteady state approach, as reported by [1]. The Chimera grid system of the URANS model consisted of 11.1 million cells, with the same grid topology as the AH-1/OLS case in [1]. This computation was run on 360 cores distributed over 9 nodes and took about 2.1 days to complete 5 rotor revolutions.

In the mid-fidelity analysis, the computational blade model is composed of 8 panels in the chordwise direction and 20 panels in the spanwise direction, identical to the discretization used in the Caradonna-Tung rotor simulations III.B. The 2D viscous database was obtained from the CHAMPS solver, covering an appropriate range of Reynolds numbers  $(1.5 \times 10^6 \le \text{Re} \le 1.5 \times 10^7)$ , Mach numbers  $(0.01 \le \text{M} \le 0.8)$ , and angles of attack ranging from  $-180^\circ$  to  $180^\circ$ . Fig. 11 illustrates the dependence of the lift and drag coefficients on the angle of attack and Mach numbers at a Reynolds number of  $1.5 \times 10^7$  for the OLS/TAAT airfoil.

Fig. 12 presents the time history of the thrust coefficient predicted by the NL-UVLM-VPM solver and the URANS solution during the forward flight simulation. For clarity, only the results from the first ten rotor revolutions are shown. After approximately two revolutions, both approaches reach a quasi-periodic state, exhibiting nearly identical amplitudes

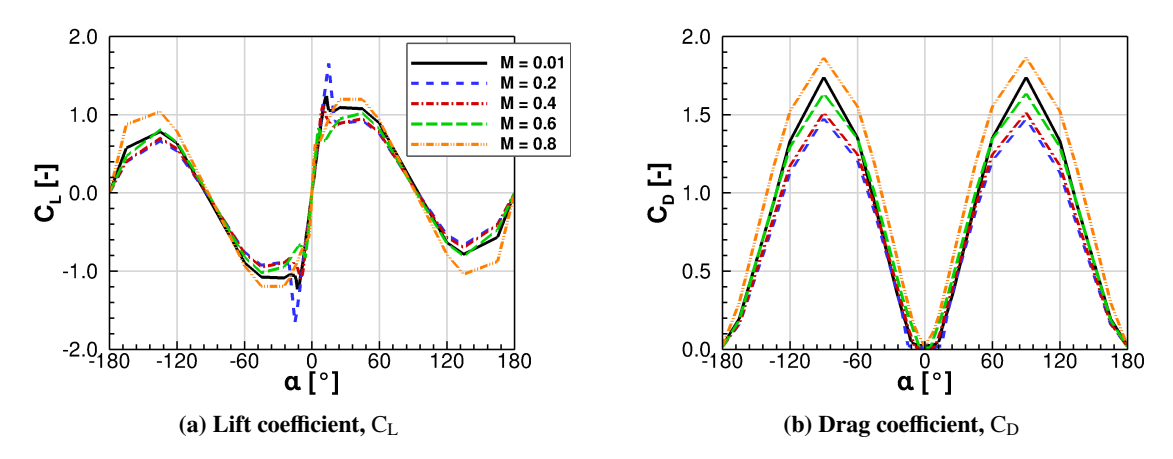


Fig. 11 OLS/TAAT airfoil aerodynamic coefficients at Re =  $1.5 \times 10^7$ .

and phase variations. The two curves remain highly overlapped throughout subsequent revolutions, indicating that the present mid-fidelity method successfully reproduces the unsteady aerodynamic response captured by the URANS solver.

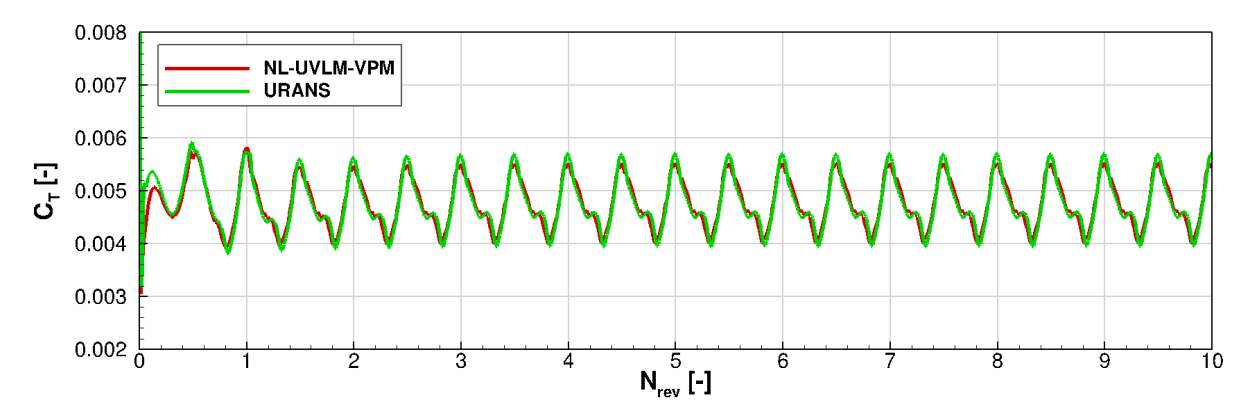


Fig. 12 Time history of the integrated thrust coefficient  $C_T$  over 10 rotor revolutions for the AH-1G rotor in forward flight.

For comparison with the flight test data, the URANS and NL-UVLM-VPM thrust coefficients were smoothed using a simple moving average (SMA) method. This post-processing procedure eliminates oscillations and enables a direct comparison of the average aerodynamic trends across the three datasets. As summarized in Table. 6, all numerical results slightly overpredict the  $C_T$  value related to the flight test measurements, while the NL-UVLM-VPM approach provides a  $C_T$  value that is highly correlated to that of the URANS results, confirming its reliability for predicting overall thrust performance in forward flight.

To assess the accuracy of the mid-fidelity simulation at a local level. Fig. 13 shows the chordwise pressure coefficient distributions at several azimuthal positions ( $\psi = 75^{\circ}$ ,  $90^{\circ}$ ,  $105^{\circ}$ ,  $270^{\circ}$ ,  $285^{\circ}$ , and  $300^{\circ}$ ) for the specific radial station (r/R = 0.91). Overall, the NL-UVLM-VPM predictions agree well with the flight measurements and URANS results at

Table 6 Integrated thrust coefficient comparisons

Method	$C_T$	Errors
Experiment[34]	0.00464	-
URANS	0.00476	2.6%
NL-UVLM-VPM	0.00478	3.0%

each azimuth. On the advancing side, both URANS and NL-UVLM-VPM solutions capture the suction peak near the leading edge, which is associated with the high dynamic pressure as the advancing blade experiences the maximum relative inflow velocity. However, both numerical methods slightly underpredict the magnitude of the suction peak compared with the experimental data. On the retreating side, the experimental data show a strong suction spike near the leading edge, followed by rapid pressure recovery. The URANS solution reproduces this overshoot more clearly, while the NL-UVLM-VPM provides a weaker peak. Despite this, both numerical results follow the overall pressure recovery and remain in quantitative agreement with the test data.

Following the comparison of the chordwise pressure distributions, the sectional aerodynamic loading is analyzed to evaluate the unsteady thrust characteristics predicted by the mid-fidelity solver. Fig. 14 illustrates the variation of the sectional thrust coefficient at two radial stations (r/R = 0.75 and 0.91) over a complete rotor revolution. The NL-UVLM-VPM predictions show good agreement with both the flight test measurements and URANS simulations in terms of magnitude and phase. The results demonstrate a good correlation between the predicted thrust coefficient variations and the experimental data for azimuthal angles ranging from  $90^{\circ}$  to  $300^{\circ}$ , indicating that the mid-fidelity approach can capture the primary unsteady aerodynamic response over most of the revolution. However, both the NL-UVLM-VPM and URANS predictions show overestimations on the advancing side ( $0^{\circ}$  to  $90^{\circ}$ ) and on the retreating side ( $300^{\circ}$  to  $360^{\circ}$ ). These discrepancies observed in these ranges are likely related to the absence of aeroelastic effects on the rotor blades in the present simulation, which can alter the effective angle of attack and the phase of the blade loads during flight. Furthermore, the influence of blade-vortex interaction (BVI) on the sectional thrust distribution is evident on the advancing side at azimuthal angles of approximately  $60^{\circ}$  to  $120^{\circ}$  and around  $300^{\circ}$  on the retreating side; however, the intensity of these BVI-induced fluctuations is underestimated. In contrast, the URANS results fail to capture these features due to numerical dissipation, highlighting the advantage of the Lagrangian vortex-particle treatment in preserving wake structures.

In addition to the aerodynamic analysis, the global wake topology is further analyzed to assess the ability of the mid-fidelity approach to capture the essential flow physics. The vortex particles are colored by the intensity of the turbulent viscosity  $\nu_t$ . Fig. 15 shows the wake structure represented by the vortex particles. It can be seen that the roll-up wake on the advancing and retreating sides, as well as the subsequent convection downstream, is successfully captured. In the forward rotor region, the wake is raised towards the rotor disk due to the upwash velocity induced by the tip vortices. Moreover, the blade-tip vortices shed from each blade interact with the subsequent blades, producing

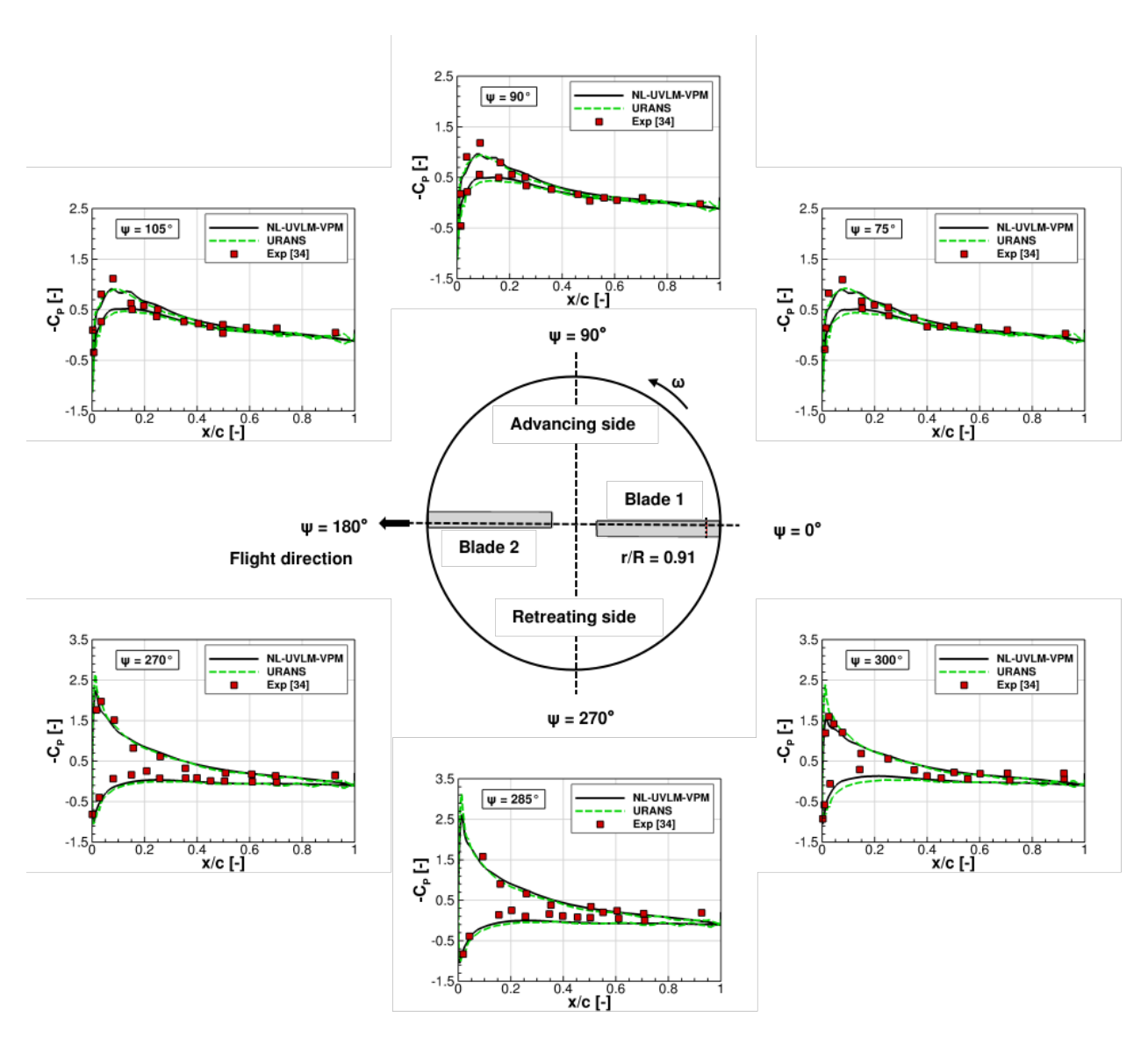


Fig. 13 Pressure coefficient distribution at r/R = 0.91 for AH-1G main rotor in forward flight.

distinct blade-vortex interactions accompanied by localized increases in  $\nu_t$ .

# D. Multi-rotor interaction case: Large-scale side-by-side rotor

Building upon the previous single-rotor validations, this section extends the assessment of the mid-fidelity approach to multi-rotor configurations. Experimental data from Sweet's side-by-side rotor in hover [35] are used for validation.

The rotor system consisted of two identical, side-by-side large-scale rotor models, each featuring two untwisted, untapered rectangular blades with a NACA 0012 airfoil. The test incorporated two rotor systems with low- and high-solidity designs. This work focuses on the high-solidity rotor system, with a rotor diameter of 15.25 feet and a chord length of 1.16 feet. The rotor operated at a constant rotational speed of 626.18 RPM (equivalent to a blade tip Mach number of 0.448). The side-by-side rotor configuration comprised two counter-rotating rotor models with an

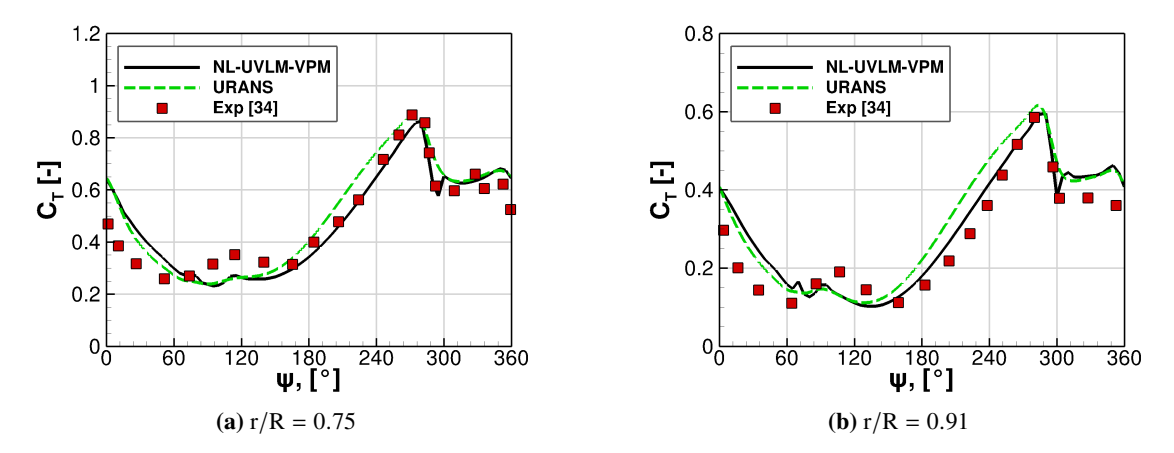


Fig. 14 Blade sectional thrust coefficients history over one rotor revolution.

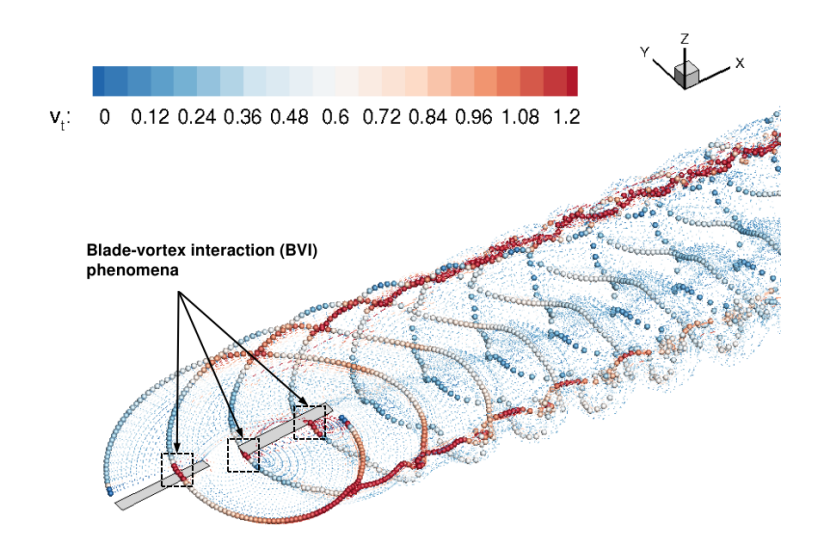


Fig. 15 Wake structures of AH-1G main rotor in forward flight.

overlap ratio of L/R = 2.03, and a phase difference of  $90^{\circ}$ , as illustrated in Fig. 16.

In the high-fidelity analysis, the time-accurate URANS simulation was conducted at a collective pitch angle of  $\theta_c = 8^{\circ}$ . The computational setup employed a Chimera grid system consisting of approximately 17.3 million cells, comprising one far-field background grid, one uniform near-field grid, and four body-fitted blade grids, as illustrated in Fig. 17. The near-field grid was refined with a grid spacing of 0.07c to adequately resolve the blade tip vortices. The simulation was executed on 640 processor cores distributed over 16 computational nodes, requiring about three days to complete five rotor revolutions.

The mid-fidelity simulations were conducted for two configurations: a single-rotor case serving as the baseline reference and a side-by-side rotor configuration (L/R = 2.03) used to validate rotor–rotor aerodynamic interactions.

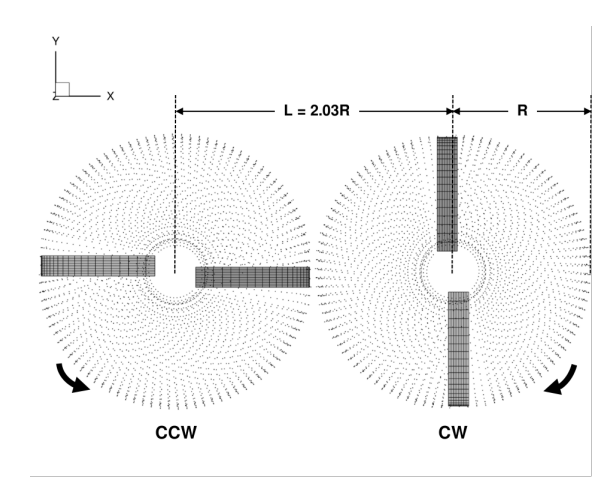


Fig. 16 Side-by-side rotor configuration, L/R = 2.03.

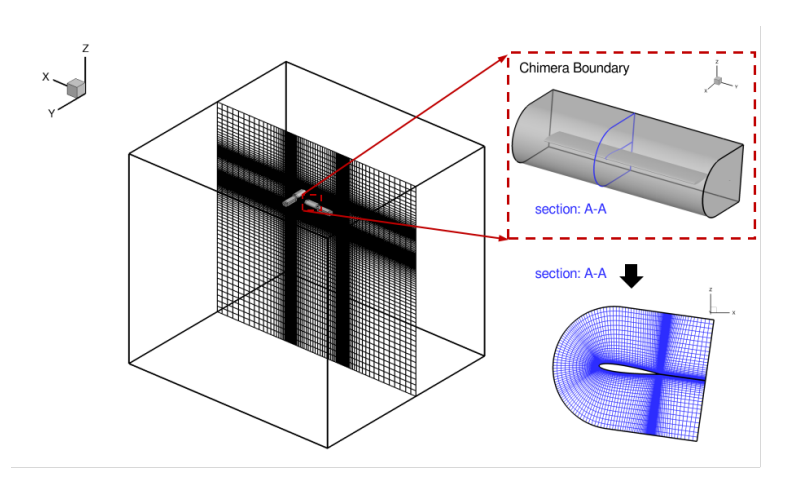


Fig. 17 URANS grid system for the side-by-side rotor system (L/R = 2.03).

Hover flight conditions with varying collective pitch angles were considered to evaluate the aerodynamic performance under different loading levels. Similar to the C-T rotor setup, each blade was discretized into an  $8 \times 20$  panel mesh (uniform in the chordwise direction and sine-spaced in the spanwise direction), providing a balance between accuracy and computational efficiency. The simulations were performed for a total of 20 rotor revolutions, including three slow-startup revolutions ( $N_s = 3$ ) to ensure smooth wake development and numerical stability.

Fig. 18 compares the aerodynamic performance of the side-by-side rotor configuration (L/R = 2.03) as predicted by the NL-UVLM-VPM solver, the high-fidelity URANS simulation, and the experimental data from Sweet [35]. The relationships between the thrust and torque coefficients ( $C_T$ - $C_Q$ ) and the figure of merit (FM) are presented. Overall, the NL-UVLM-VPM predictions are in close agreement with both the experimental and URANS results across the entire range of thrust coefficients, accurately capturing the  $C_T$  and  $C_Q$  trends that characterize the induced power behavior of the side-by-side rotor system. The figure of merit (FM) comparison further demonstrates that the NL-UVLM-VPM method provides performance predictions consistent with experimental observations. At high loading conditions (large

 $C_T$ ), where URANS data are available, both URANS and NL-UVLM-VPM slightly underpredict FM compared with the experiment. This deviation may stem from the absence of aeroelastic deformation in the numerical models, which can influence rotor performance under high-thrust operation.

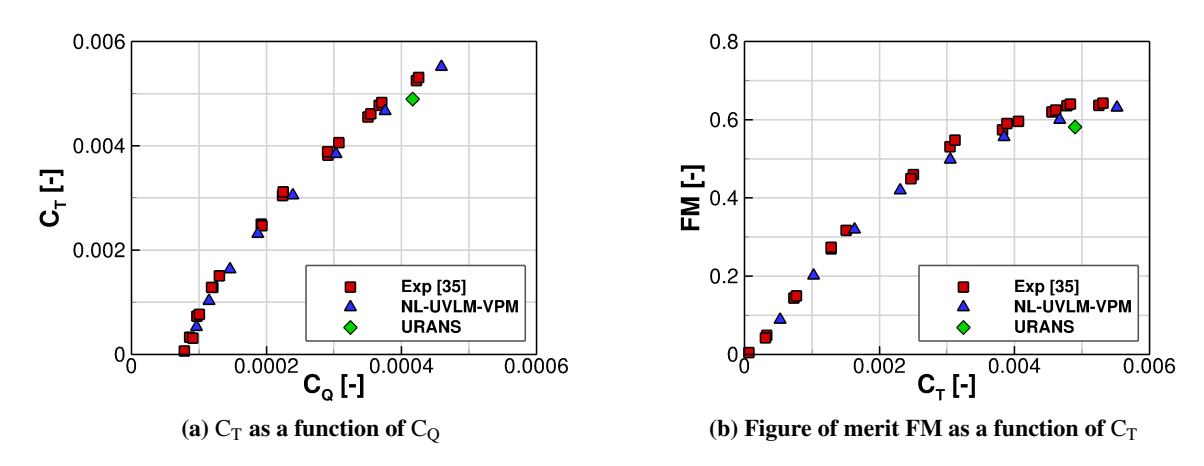


Fig. 18 Comparison of rotor performance for the side-by-side rotor model (L/R = 2.03).

Fig. 19 illustrates the spanwise distribution of the normal force coefficient ( $C_N$ ) for three rotor azimuthal phases at  $\theta_c = 8^\circ$ , obtained from the NL-UVLM-VPM simulations, with the single-rotor solution used as a reference. These results provide insight into the unsteady evolution of blade loading as the rotor interacts with the skewed wake and upwash field induced by the adjacent rotor. In this figure, the entire rotor revolution is divided into three phases: Phase 1 ( $0^\circ \le \psi \le 90^\circ$ ), corresponding to the advancing side, where the blade leaves the wake interaction region and recovers from the influence of the interaction. The  $C_N$  value experiences a moderate rise near the blade tip; Phase 2 ( $90^\circ \le \psi \le 270^\circ$ ), covers the transition from the advancing to the retreating side, where the blade is largely out of the interference zone and experiences the lowest induced disturbance from the neighboring rotor. Here, the  $C_N$  value remains relatively stable and close to the single-rotor reference across the span; and Phase 3 ( $270^\circ \le \psi \le 360^\circ$ ), corresponding to the re-entry through the retreating side where the blade encounters the induced wake region of the adjacent rotor again. The  $C_N$  value undergoes a gradual rise in the inboard regions and a noticeable drop in the outboard regions due to renewed interference.

The colormaps of the instantaneous axial velocity fields at  $N_{rev} = 10$ , along with the velocity profiles extracted at z/R = -0.5 and z/R = -1.0, are displayed in Fig. 20, where the URANS results are included for comparison. The contours clearly reveal two dominant downwash regions beneath each rotor, separated by a weaker interaction zone between them. As the flow convects downstream, these downwash cores move closer and merge slightly, indicating wake contraction and the onset of mutual induction between the rotors, which leads to a mildly asymmetric velocity distribution with localized upwash in the midplane. The velocity profiles on the right of Fig. 20 provide a more quantitative comparison of NL-UVLM-VPM predictions and URANS results. It can be seen that both methods capture

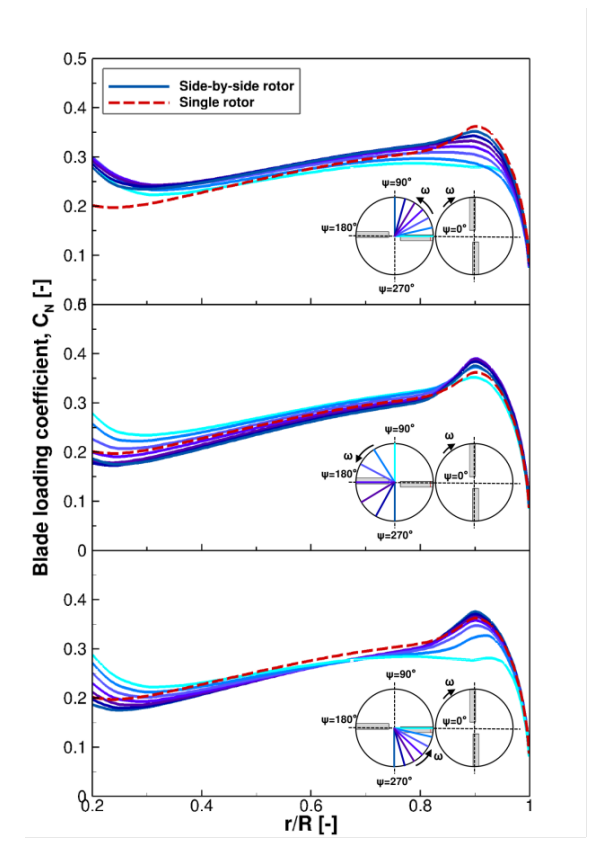


Fig. 19 Blade loading as blade goes through region of wake skewness and accentuated upwash between the rotors.

the magnitude and position of the downwash peaks generated by the tip vortices, demonstrating that the proposed mid-fidelity model accurately reproduces the wake contraction and inter-rotor interaction effects observed in the high-fidelity solution.

Figure 21 compares the instantaneous vortical structures of the side-by-side rotor configuration predicted by the NL-UVLM-VPM with URANS simulations at  $N_{rev} = 10$ . In the NL-UVLM-VPM results, the geometric characteristics of the vortex wake are first determined, followed by the computation of the induced velocity distribution. The resulting vortex structures are then identified using the Q-criterion, as shown in Fig. 21a. Similarly, Fig. 21b presents the vorticity field from the URANS solution, with the vortex structures extracted using the same Q-criterion. In both cases, the Q value is consistently set to 0.005 to depict the overall wake topology and rotor-rotor interactions clearly.

Both simulations capture coherent helical tip vortices that roll up and convect downstream. The two wake systems show a distinct inward contraction, confirming the presence of mutual induction between the rotors. This interaction produces a skewed wake geometry in which the inner vortices are drawn upward and toward the midplane, while the outer vortices are deflected inward due to global wake contraction. The NL-UVLM-VPM method accurately reproduces the dominant wake behavior, including tip-vortex roll-up, rotor mutual interaction, and wake skewness. These alignments

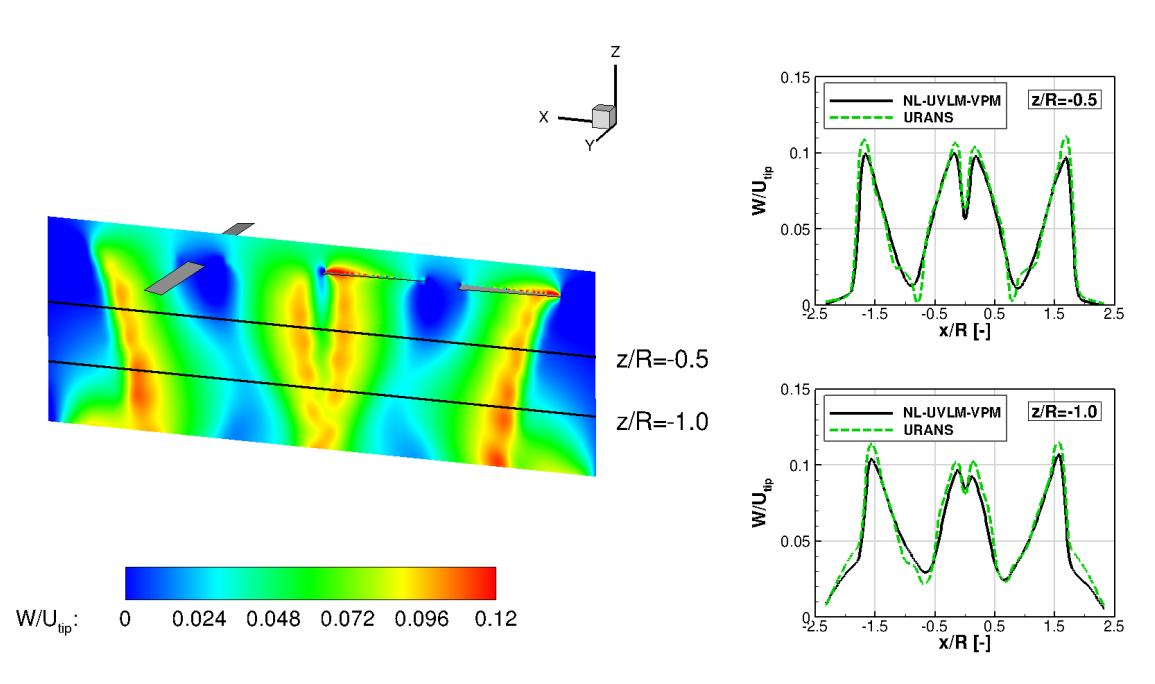


Fig. 20 Contour of the instantaneous velocity along the z-axis and velocity profiles extracted at z/R = -0.5 and -1.0.

confirm that the mid-fidelity NL-UVLM-VPM approach effectively replicates the essential physics of wake interactions, providing a reliable alternative to high-fidelity URANS simulations for the problems of multi-rotor interaction.

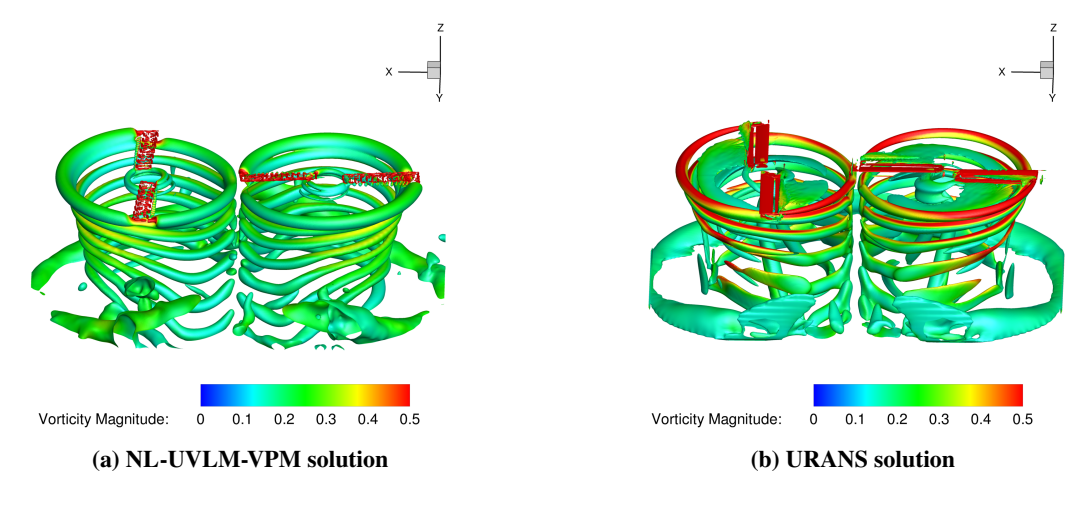


Fig. 21 Comparison between vortical structures obtained from NL-UVLM-VPM and URANS calculations.

# E. Computational time

In this work, the computations were primarily conducted on the Niagara high-performance cluster at Compute Canada, which consists of 2024 nodes, each equipped with 40 Intel "Skylake" cores at 2.4 GHz, interconnected via an EDR Infiniband network. To assess the computational efficiency of the mid-fidelity approach, the average CPU time per revolution for both the NL-UVLM-VPM and high-fidelity URANS computations over all three benchmark cases

is summarized in Table 7. As observed, the NL-UVLM-VPM approach presents substantially higher efficiency than the URANS simulations, achieving a speedup ratio exceeding 140. This significant reduction in computational cost demonstrates the efficiency of the mid-fidelity approach in this study while maintaining good agreement with high-fidelity URANS in terms of aerodynamic force predictions and near-field flow features, including the flow distribution and instantaneous Q-criterion structures.

Table 7 CPU run-time of two approaches for all three test cases simulations

Test case	Approach	CPU cores	CPUh/rev	Speedup
C-T rotor	NL-UVLM-VPM	40	26	147.2
	URANS	240	3827	1.0
AH-1G rotor	NL-UVLM-VPM	40	25	142.4
	URANS	360	3560	1.0
Side-by-side rotor	NL-UVLM-VPM	40	53	173.9
	URANS	640	9216	1.0

#### IV. Conclusions

This study presents a mid-fidelity aerodynamic tool based on the NL-UVLM-VPM approach, aimed at delivering a rapid and reliable assessment of helicopter rotor aerodynamic performance. It integrates the unsteady vortex-lattice method with a high-fidelity RANS database via the  $\alpha$ -coupling algorithm to improve the computation of unsteady aerodynamic loads on the rotor blades and employs a vortex particle method with an additional LES viscosity diffusion term to stabilize the development of the rotor wake, enabling the resolution of the wake coherent, transient, and turbulent breakdown regions. To facilitate simulations of complex flight regimes and multi-rotor interactions, the tool includes algorithmic enhancements such as an adaptive wake-particle conversion technique, which improves computational efficiency by nearly 70% and a multiple-reference-frame kinematic formulation supporting diverse rotor-blade motions, including forward flight.

This mid-fidelity approach was validated against high-fidelity URANS simulations and experimental data in three representative scenarios: hover, forward flight, and side-by-side rotor interaction. Results show that the method can accurately predict critical aerodynamic metrics, including thrust and torque coefficients, sectional blade loads, tip vortex trajectories, and wake contraction and skewness. The predicted flow field agrees well with the URANS results, maintaining physical consistency in vortex roll-up and mutual interaction effects.

Computationally, this mid-fidelity tool reduces CPU time by over two orders of magnitude compared to URANS, highlighting its capabilities in parametric studies, design optimization, and unsteady wake analysis. This method achieves an effective balance between physical accuracy and computational efficiency, serving as a reliable predictive tool for rotorcraft aerodynamics.

In the future, research will focus on applying the present mid-fidelity method to helicopter rotor blades with complex

tip geometries using the 2.5D hypothesis [38], as well as extending this tool by integrating the panel method to analyze rotor-fuselage interactions. Multi-disciplinary effects, such as aeroelasticity or aero-icing, could also be incorporated straightforwardly due to the stripwise  $\alpha$ -coupling approach.

# Acknowledgments

The authors would like to thank Baptiste Arnould for his assistance with the CHAMPS Solver. This work was supported by the Natural Sciences and Engineering Research Council of Canada (NSERC), the Consortium de recherche et d'innovation en aérospatiale au Québec (CRIAQ), and CAE Inc. under the NSERC Alliance Grant (No. ALLRP 572207-22) and the CRIAQ project HAMAC. Calculations were performed on the Digital Research Alliance of Canada and Calcul Québec clusters. Lastly, we acknowledge the use of ChatGPT (GPT-5, 2025) for language polishing and editing.

#### References

- [1] Fu, J., and Vigevano, L., "An Efficient Helicopter Main Rotor Trim Method Based on Computational Fluid Dynamics," 49th European Rotorcraft Forum, Bückeburg, Germany, 2023.
- [2] Chaderjian, N. M., and Ahmad, J. U., "Detached Eddy Simulation of the UH-60 Rotor Wake using Adaptive Mesh Refinement," American Helicopter Society 68th Annual Forum, Fort Worth, USA, 2012.
- [3] Narducci, R., "Hover Performance Assessment of Several Tip Shapes Using OVERFLOW," 53rd AIAA Aerospace Sciences Meeting, AIAA, Kissimmee, USA, 2015.
- [4] Jain, R., "Hover Predictions for the S-76 Rotor with Tip Shape Variation Using CREATE-AV Helios," *53rd AIAA Aerospace Sciences Meeting*, AIAA, Kissimmee, USA, 2015.
- [5] Zhao, J., and He, C., "A Viscous Vortex Particle Model for Rotor Wake and Interference Analysis," *Journal of the American Helicopter Society*, Vol. 50, No. 1, 2010. https://doi.org/10.4050/JAHS.55.012007.
- [6] Tan, J., and Wang, H., "Simulating Unsteady Aerodynamics of Helicopter Rotor with Panel/Viscous Vortex Particle Method," Aerospace Science and Technology, Vol. 30, No. 1, 2013, pp. 255–268. https://doi.org/10.1016/j.ast.2013.08.010.
- [7] Lee, H., and Lee, D. J., "Numerical Investigation of the Aerodynamics and Wake Structures of Horizontal Axis Wind Turbines by Using Nonlinear Vortex Lattice Method," *Renewable Energy*, Vol. 132, 2019, pp. 1121–1133. https://doi.org/10.1016/j.renene.2018.08.087.
- [8] Tugnoli, M., Montagnani, D., Syal, M., Droandi, G., and Zanotti, A., "Mid-fidelity Approach to Aerodynamic Simulations of Unconventional VTOL Aircraft Configurations," *Aerospace Science and Technology*, Vol. 115, 2021. https://doi.org/10.1016/j. ast.2021.106804.

- [9] Alvarez, E. J., and Ning, A., "Stable Vortex Particle Method Formulation for Meshless Large-Eddy Simulation," *AIAA Journal*, Vol. 62, No. 2, 2024, pp. 637–656. https://doi.org/10.2514/1.J063045.
- [10] Alvarez, E. J., and Ning, A., "Modeling Multirotor Aerodynamic Interactions Through the Vortex Particle Method," *AIAA Aviation 2019 Forum*, AIAA, Dallas, USA, 2019.
- [11] Proulx-Cabana, V., and Laurendeau, E., "Towards Non-Linear Unsteady Vortex Lattice Method (NL-UVLM) for Rotary-Wing Aerodynamics," *Proceedings of the CASI AERO*, Montreal, Canada, 2019.
- [12] Cocco, A., Savino, A., Colli, A., Masarati, P., and Zanotti, A., "A Non-Linear Unsteady Vortex-Lattice Method for Rotorcraft Applications," *The Aeronautical Journal*, Vol. 128, No. 1328, 2024, pp. 2308–2330. https://doi.org/10.1017/aer.2024.55.
- [13] Samad, A., Tagawa, G. B. S., Morency, F., and Volat, C., "Predicting Rotor Heat Transfer Using the Viscous Blade Element Momentum Theory and Unsteady Vortex Lattice Method," *Aerospace*, Vol. 7, No. 7, 2020. https://doi.org/10.3390/ aerospace7070090.
- [14] Gallay, S., and Laurendeau, E., "Nonlinear Generalized Lifting-Line Coupling Algorithms for Pre/Poststall Flows," *AIAA Journal*, Vol. 53, No. 7, 2015, pp. 1784–1792. https://doi.org/10.2514/1.J053530.
- [15] Bhagwat, M. J., and G. L. J., "Generalized Viscous Vortex Model for Application to Free-Vortex Wake and Aeroacoustic Calculations," *The 58th Annual Forum and Technology Display of the American Helicopter Society International*, Montreal, Canada, 2002.
- [16] Ferlisi, C., "Rotor wake modelling using the vortex-lattice method," Master's thesis, École Polytechnique de Montréal, Montréal, Canada, 2018.
- [17] Valentin, J., and Bernardos, L., "Validation of A New Solver Based on the Vortex Particle Method for Wings, Propellers and Rotors," 49th European Rotorcraft Forum, Bückeburg, Germany, 2023.
- [18] Parenteau, M., Bourgault-Cote, S., Plante, F., and Laurendeau, E., "Development of Parallel CFD Applications on Distributed Memory with Chapel," 34th IEEE International Parallel and Distributed Processing Symposium Workshops (IPDPSW 2020), New Orleans, USA, 2020.
- [19] Proulx-Cabana, V., Nguyen, M. T., Prothin, S., Michon, G., and Laurendeau, E., "A Hybrid Non-Linear Unsteady Vortex Lattice-Vortex Particle Method for Rotor Blades Aerodynamic Simulations," *Fluids*, Vol. 7, No. 2, 2022. https://doi.org/10. 3390/aerospace7070090.
- [20] Katz, J., and Plotkin, A., Low-Speed Aerodynamics, 2nd ed., Cambridge University Press, Cambridge, 2001.
- [21] Vatistas, G. H., Kozel, V., and Mih, W. C., "A Simpler Model for Concentrated Vortices," *Experiments in Fluids*, Vol. 11, No. 1, 1991, pp. 73–76. https://doi.org/10.1007/BF00198434.
- [22] Simpson, R. J., Palacios, R., and Murua, J., "Induced-Drag Calculations in the Unsteady Vortex Lattice Method," *AIAA Journal*, Vol. 51, No. 7, 2013, pp. 1775–1779. https://doi.org/10.2514/1.J052136.

- [23] Beale, J. T., "A Convergent 3-D Vortex Method with Grid-Free Stretching," *Mathematics of Computation*, Vol. 46, No. 174, 1986, pp. 401–424. https://doi.org/10.2307/2007984.
- [24] Wincklemans, G. S., "Topic in Vortex Methods for the Computation of Three- and Two-Dimensional Incompressible Unsteady Flows," Ph.d. thesis, California Institute of Technology, California, USA, 1989.
- [25] Williamson, J. H., "Low-Storage Runge-Kutta Schemes," *Journal of Computational Physics*, Vol. 35, No. 1, 1980, pp. 48–56. https://doi.org/10.1016/0021-9991(80)90033-9.
- [26] Kolmogorov, A. N., "The Local Structure of Turbulence in Incompressible Viscous Fluid for Very Large Reynolds Numbers," *Proceedings of the Royal Society A*, Vol. 434, No. 1890, 1991, pp. 9–13. https://doi.org/10.1098/rspa.1991.0075.
- [27] Vreman, A. W., "An Eddy-Viscosity Subgrid-Scale Model for Turbulent Shear Flow: Algebraic Theory and Applications," *Physics of Fluids*, Vol. 16, No. 10, 2004, pp. 3670–3681. https://doi.org/10.1063/1.1785131.
- [28] Parenteau, M., Bourgault-Cote, S., Plante, F., Kayraklioglu, E., and Laurendeau, E., "Development of Parallel CFD Applications with the Chapel Programming Language," *AIAA Scitech 2021 Forum*, Virtual Event, 2021.
- [29] Biava, M., and Vigevano, L., "Simulation of a Complete Helicopter: a CFD Approach to the Study of Interference Effects," *Aerospace Science and Technology*, Vol. 19, No. 1, 2012, pp. 37–49. https://doi.org/10.1016/j.ast.2011.08.006.
- [30] Roe, P. L., "Approximate Riemann Solvers, Parameter Vectors, and Difference Schemes," *Journal of Computational Physics*, Vol. 43, No. 2, 1981, pp. 357–372. https://doi.org/10.1016/0021-9991(81)90128-5.
- [31] Venkatakrishnan, V., "On the Accuracy of Limiters and Convergence to Steady State Solutions," 31st Aerospace Sciences Meeting, Reno, USA, 1993.
- [32] Chesshire, G., and Henshaw, W. D., "Composite Overlapping Meshes for the Solution of Partial Differential Equations," *Journal of Computational Physics*, Vol. 90, No. 1, 1990, pp. 1–64. https://doi.org/10.1016/0021-9991(90)90196-8.
- [33] Caradonna, F. X., and Tung, C., "Experimental and Analytical Studies of a Model Helicopter Rotor in Hover," *NASA TM-81232*, 1981.
- [34] Cross, J. L., and Watts, M. E., "Tip Aerodynamics and Acoustic Test A Report and Data Survey," NASA RP-1179, 1988.
- [35] Sweet, G. E., "Hovering Measurements for Twin-Rotor Configurations With and Without Overlap," NASA TN-D-534, 1960.
- [36] Chung, K. H., Kim, J. W., Ryu, K. W., Lee, K. T., and J. L. D., "Sound Generation and Radiation from Rotor Tip-Vortex Pairing Phenomenon," *AIAA Journal*, Vol. 44, No. 6, 2006, pp. 1181–1187. https://doi.org/10.2514/1.22548.
- [37] Fu, J., Yuan, Y., and Vigevano, L., "Numerical Investigations of the Vortex Feature-Based Vorticity Confinement Models for the Assessment in Three-Dimensional Vortex-Dominated Flows," *Meccanica*, Vol. 57, 2022, pp. 1657–1676. https://doi.org/10.1007/s11012-022-01525-5.

[38] Lavoie, P., Bourgault-Côté, S., and Laurendeau, E., "Numerical algorithms for infinite swept wing ice accretion," *Computers & Fluids*, Vol. 161, 2018, pp. 189–198. https://doi.org/10.1016/j.compfluid.2017.11.015.